

# MODELLING MICROSILICA PARTICLE FORMATION AND GROWTH DUE TO THE COMBUSTION REACTION OF SILICON MONOXIDE WITH OXYGEN\*

RAQUEL GONZÁLEZ-FARIÑA<sup>†</sup>, ANDREAS MÜNCH<sup>†</sup>, JAMES M. OLIVER<sup>‡</sup>, AND ROBERT A. VAN GORDER<sup>‡</sup>

**Abstract.** Microsilica particles arise as a byproduct of silicon furnace operation, created inside high temperature flames due to the combustion reaction of silicon monoxide with oxygen. These nanoparticles, which grow as silicon dioxide vapour condenses on the surface of existing particles, are used in a variety of composite materials. The size and quality of the particles affect the performance of the material used for such applications, and hence control of these quantities is of importance to manufacturers. Motivated by this, we derive a mathematical model that connects local thermal and chemical concentrations conditions to the formation and growth of microsilica particles. We consider two distinct reductions of our general model: the case of initially well-mixed or spatially homogeneous chemical species (modelling the region within the flame or reaction zone), and the case of initially spatially separated chemical species, in which diffusion will play a dominant role in providing material to a combustion front (modelling a larger cross section, which contains a reaction zone with limiting quantities of fuel which must diffuse into the reaction zone). In both cases, we provide asymptotic solutions for the temperature, chemical concentrations, and number density function of microsilica particles in the oxygen rich limit, and compare them to numerical simulations. Motivated by realistic furnace control mechanisms, we treat the relative quantity of oxygen to other fuel components and the saturation concentration of silicon dioxide as a control parameters, discussing how each may be used to modify the properties (such as size and abundance) of microsilica particles formed. One physically interesting finding is the theoretical description of a bimodal distribution for microsilica particle size which was previously observed in experiments.

**Key word.** particle growth, reaction-diffusion systems, asymptotic analysis, moment equations, microsilica, silica fume

**AMS subject classifications.** 35Q79, 35C20, 35Q70, 80A32, 80M35

**1. Introduction.** Microsilica or silica fume is a byproduct of the silicon and ferrosilicon industry. It consists mainly of spherical particles of amorphous  $\text{SiO}_2$  with more than 95% of them being finer than  $1\mu\text{m}$  [32] (see Figure 1). These particles mainly grow by condensation but can also form aggregates and agglomerates as discussed below. The primary industrial use of microsilica is as an additive in high performance concrete, but is also utilised for refractories and polymers. Modifications in the silicon production process affect not only the microsilica yield, but also the quality and properties of the particle. Depending on the application, certain particle sizes or surface areas are preferred [10], and as such, there is a need to study which conditions are favourable for microsilica formation and growth.

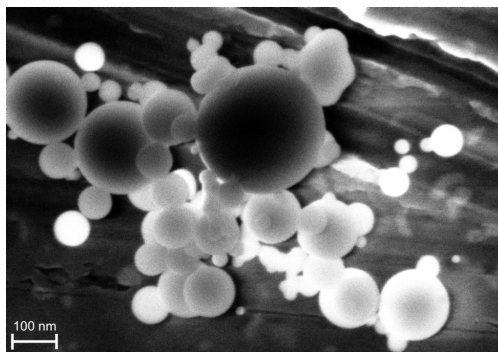


Fig. 1: SEM image of microsilica particles (provided by Elkem [12]). The majority of the particles are perfectly spherical and form agglomerates (weak bonds), while a small percentage form aggregates (some with irregular shape as in the top right corner).

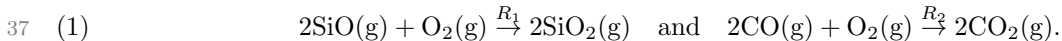
Microsilica particles are formed inside high temperature flames due to the combustion of  $\text{SiO}$  gas with

\*This publication is based on work supported by the EPSRC Center for Doctoral Training in Industrially Focused Mathematical Modelling (EP/L015803/1) in collaboration with Elkem

<sup>†</sup>Mathematical Institute, University of Oxford, Andrew Wiles Building, Radcliffe Observatory Quarter, Woodstock Road, Oxford, OX2 6GG, United Kingdom

<sup>‡</sup>Department of Mathematics and Statistics, University of Otago, P.O. Box 56, Dunedin 9054, New Zealand ([rvan-gorder@maths.otago.ac.nz](mailto:rvan-gorder@maths.otago.ac.nz))

oxygen, which is a byproduct of the quartz reduction process to obtain silicon. Another byproduct of the process is CO gas which also combusts, producing less bright and thus less hot flames. Therefore, both chemicals, SiO and CO, compete for oxygen. In Figure 2, we provide a sketch of an industrial silicon furnace where both silicon and microsilica are produced (refer to [32, 36] for more details on the silicon manufacturing process). In some configurations, the oxygen is provided via air which enters the furnace hood through side doors, and hence the quantity of oxygen can be controlled. We focus our attention on the two exothermic combustion reactions happening in the furnace hood, namely



Before the particles form, SiO<sub>2</sub> is in a vapour phase, which can be treated as an ideal gas. When this vapour reaches saturation, it undergoes a change of state from gas into solid that also releases energy and under which the particles form. After nucleation, the growth of the primary particles is purely by condensation, that is, by molecular addition of mass to the surface of existing particles, which is the main focus of this paper. Additionally, some small percentage of the primary particles created show aggregation, like the one attached to the top of the largest particle in Figure 1 with an irregular shape. In later stages of the process, when microsilica is collected, a high percentage of particles agglomerate via weak inter-particle forces, as can be seen from Figure 1 where most particles are attached to each other. Since aggregation does not occur frequently, and agglomeration at late stages is not very relevant to industrial scale production (since the weak bonds can be broken easily with a dispersing machine [11]), we will not study these mechanisms in this work and will only focus on the formation and growth of the primary particles through condensation.

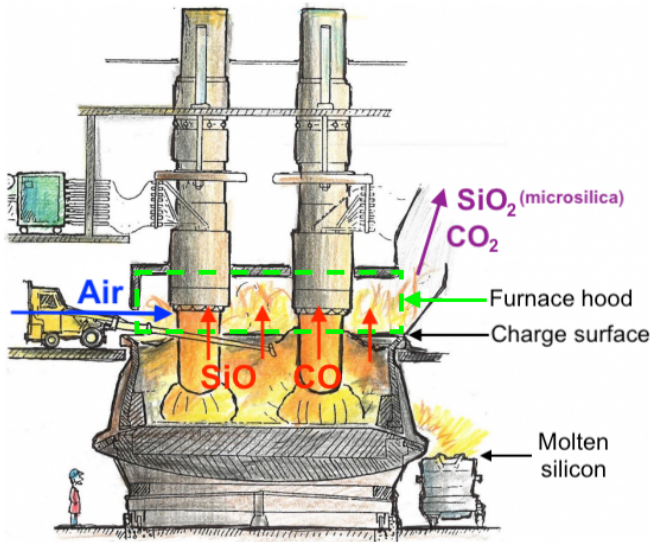


Fig. 2: Sketch of a silicon furnace indicating the location of the furnace hood (green dashed square), that is, where the combustion reactions (1) happen. Reproduced from The Si Process Drawings, by Thorsteinn Hannesson.

Several mathematical models [15, 23, 35, 36] have been developed for the heat and mass balances, chemical reactions, and thermodynamics within silicon furnaces. These models may be used to predict the behaviour of the furnace below the charge surface where the reduction of quartz occurs, resulting in molten silicon which then exits the furnace, is collected, and solidifies into usable product [6]. Far less attention has been focused on modelling processes inside the combustion chamber which lead to the creation of microsilica, yet this too is of industrial use. In [18], NO formation is considered at different parts of the silicon process (in the absence of chemical reactions), which is strongly correlated to the formation of silica fume. A similar model is introduced in [17] which is also coupled to chemical reactions due to the combustion of the off-gases, however, this model captures the dynamics of taphole gases during the tapping of the silicon, which is slightly different from the physics and chemistry involved in a furnace hood.

59 Although the application is different, literature on the formation and growth of aerosol particles will be  
60 useful in motivating aspects of our model. When studying aerosols, a common approach is to use population  
61 balance equations to model physical mechanisms including nucleation, continuous growth, coagulation, and  
62 breakage within a population of particles with different sizes [31], in order to predict particle size distribu-  
63 tion and other properties. Flagan and Lunden [13] considered growth of nanoparticles by coagulation and  
64 coalescence from the vapour phase, giving expressions for the Brownian collision rates for both spherical  
65 particles and complex agglomerate structures. Pratsinis [29] considered a model for simultaneous nucleation,  
66 condensation, and coagulation in aerosol reactors, in terms of the moments of the aerosol size distribution.  
67 Surface reaction is another common growth mechanism, and Artelt *et al.* [3] studied the formation and  
68 growth of titania particles from the vapour phase, concluding that reaction on the surface of existing  $\text{TiO}_2$   
69 is the dominant growth mechanism. Similar studies on nucleation and growth of fine particles have been  
70 undertaken for MgO smoke [38] and microalumina particles [4]; the latter explores how the condensation  
71 reaction depends on thermal effects by deriving equations for the number density of each reacting species  
72 and for the temperature. We adopt this approach for our model, focusing on the continuous growth of the  
73 particles by condensation as the growth mechanism. There exist population balance models in the litera-  
74 ture for the formation of silica particles from the gas phase [20, 33, 34], yet in these cases silica particles are  
75 generated under different conditions than the ones in this study and therefore their properties, formation,  
76 and growth mechanisms are slightly different.

77 Existing models for particle formation via combustion use simplified profiles and equations for the  
78 chemicals and temperature variations in the combustion chamber, leading to chemical models which are  
79 uncoupled or one way coupled with the particle growth mechanism. In this work, we present a fully coupled  
80 system that includes the effects of the chemical concentrations and temperature differences on the particles,  
81 and vice versa. Motivated by studies carried out on heat and mass balances, chemical reactions, and  
82 thermodynamics within silicon furnaces [35, 36], we couple a model that predicts the local temperature  
83 profiles and chemistry within the furnace hood to the population balance equation through the growth and  
84 nucleation rates. We couple the population balance equation back into the temperature and concentration  
85 of the condensed material within the furnace through source and sink terms similar to those used in [1, 24].

86 The remainder of this paper is organized as follows. In Section 2 we develop the mathematical model,  
87 and present a non-dimensional version of it under the assumption of a simplified geometry. While there are  
88 a number of parameters in our model, most are well-known, with the initial concentration of oxygen and  
89 saturation concentration of silicon dioxide being the two free parameters which we may control. In Section  
90 3 we study the well-mixed limit for all chemical species, which is a caricature of the zoomed in region within  
91 the combustion or reaction zone. In Section 4 we consider the scenario where oxygen is initially spatially  
92 segregated from the other chemical species, with a reaction boundary forming between the two. In order to  
93 gain a qualitative understanding of the heat and mass transfer problem, we obtain asymptotic solutions for  
94 both reductions of our model for an oxygen rich environment and in the limit where the feedback of particle  
95 growth on temperature and chemistry is small, while we consider numerical simulations for more general  
96 parameter regimes. We discuss our results and their relevance to industrial scale production of microsilica  
97 in Section 5.

98 **2. Mathematical model.** We are interested in modelling the dynamics of the main chemical species  
99 found in the furnace hood above the charge surface:  $\text{N}_2(\text{g})$ ,  $\text{O}_2(\text{g})$ ,  $\text{SiO}(\text{g})$ ,  $\text{SiO}_2(\text{g})$ ,  $\text{CO}(\text{g})$ , and  $\text{CO}_2(\text{g})$ .  
100 Other compounds such as volatiles are not taken into account. Thus, we model the fluid as a combination  
101 of the gaseous species mentioned before, where the only chemical reactions occurring are the combustion  
102 reactions (1). We consider equations for the conservation of mass and energy coupled to a particle growth  
103 model, while greatly simplifying the flow problem by choosing the velocity of the fluid to be uniform in  
104 space and time on an unbounded spatial domain. For such a configuration, the velocity can be scaled out  
105 with a change of space variable moving with the flow. Subsequent work will consider more realistic flow  
106 regimes, but for now these assumptions are sufficient to study the regions local to a reaction zone where the  
107 microsilica is produced, as is the focus of this paper.

108 **2.1. Conservation of chemical species.** The mass conservation equations express how the concen-  
109 tration of each species depends on the diffusion of species and chemical reactions. Taking  $C_X(\mathbf{x}, t)$  to be the  
110 concentration of species  $X$  in units  $\text{mol}/\text{m}^3$ , where  $\mathbf{x}$  denotes position in cartesian coordinates and  $t$  time,  
111 the governing equations are given by

$$\begin{aligned}
112 \quad (2a) \quad & \frac{\partial C_{\text{N}_2}}{\partial t} - D_{\text{N}_2} \nabla^2 C_{\text{N}_2} = 0, \\
113 \quad (2b) \quad & \frac{\partial C_{\text{O}_2}}{\partial t} - D_{\text{O}_2} \nabla^2 C_{\text{O}_2} = -R_1 - R_2, \\
114 \quad (2c) \quad & \frac{\partial C_{\text{SiO}}}{\partial t} - D_{\text{SiO}} \nabla^2 C_{\text{SiO}} = -2R_1, \\
115 \quad (2d) \quad & \frac{\partial C_{\text{SiO}_2}}{\partial t} - D_{\text{SiO}_2} \nabla^2 C_{\text{SiO}_2} = 2R_1 - S_C, \\
116 \quad (2e) \quad & \frac{\partial C_{\text{CO}}}{\partial t} - D_{\text{CO}} \nabla^2 C_{\text{CO}} = -2R_2, \\
117 \quad (2f) \quad & \frac{\partial C_{\text{CO}_2}}{\partial t} - D_{\text{CO}_2} \nabla^2 C_{\text{CO}_2} = 2R_2,
\end{aligned}$$

118 where  $D_X$  is the diffusion rate of species  $X$ ,  $R_i$ ,  $i = 1, 2$  are the source terms due to the combustion reactions  
119 given in (1), and  $S_C$  represents a sink term due to the formation of the particles which will be defined in  
120 Section 2.4. We have included conservation of the two main components in air,  $\text{N}_2$  and  $\text{O}_2$ , which appear to  
121 be in much higher concentrations than the rest of the species. In addition,  $\text{SiO}$  and  $\text{CO}$  are competing for  
122 the oxygen, while we assume the nitrogen to be nonreacting even though in some cases it could react with  
123 oxygen forming  $\text{NO}_x$  compounds. Here, we only consider the dominant reactions, but note that others could  
124 in principle be introduced to the model.

125 For elementary chemical reactions, the reaction rate is proportional to a power of the concentrations of  
126 the reactants according to the law of mass action. However, for more complex reactions simplified kinetic  
127 models are often adopted, where the powers may not be equal to the stoichiometric coefficients of the reacting  
128 species, and are often instead determined experimentally [7, 40, 44]. In our case, the combustion of  $\text{SiO}$   
129 and  $\text{CO}$  with oxygen involves some intermediate chemical reactions that are not fully understood by our  
130 industrial partners. However, since the essential nature of the process is that  $\text{SiO}$ ,  $\text{CO}$ , and oxygen are  
131 consumed while products and heat are generated, both combustion reactions are well approximated by  
132 one-step irreversible processes represented by (1). Here we consider each reaction to be first order in both  
133 reactants [12]. The reaction rates are typically highly dependent on the temperature and this is included  
134 by considering an Arrhenius term of the form  $K_i(T) = A_i \exp(-E_i/RT)$ , where  $E_i$  is the activation energy  
135 of the reaction,  $A_i$  is a pre-exponential coefficient,  $T$  is the temperature of the system, and  $R = 8.314$   
136  $\text{J}\cdot\text{mol}^{-1}\text{K}^{-1}$  is the universal gas constant. Thus, we adopt the reaction rates given by  $R_1 = K_1(T)C_{\text{SiO}}C_{\text{O}_2}$ ,  
137  $R_2 = K_2(T)C_{\text{CO}}C_{\text{O}_2}$ . Notice that we can easily express the concentrations used above in terms of partial  
138 pressures ( $P_i$ ) by using Dalton's law of partial pressures, namely  $C_i = P_i C_T / P$ , for every chemical species  $i$ ,  
139 where  $P$  is the total pressure of the fluid, and  $C_T = \sum_{\text{species } i} C_i$ . A full list of the dimensional parameters  
140 used in our model is given in Table 1.

141 **2.2. Conservation of energy.** We now consider how the temperature,  $T(\mathbf{x}, t)$ , varies in space and  
142 time. The temperature is affected by the thermal conductivity of the fluid, and by the heat released by the  
143 chemical reactions ( $S_R$ ) and the change of state due to the formation of the particles ( $S_T$ ). Thus, we have  
144 the conservation of energy equation

$$145 \quad (3) \quad \frac{\partial}{\partial t} (\rho_0 c_p T) - \nabla \cdot (\kappa \nabla T) = S_R + S_T,$$

146 where  $\rho_0$ ,  $c_p$ , and  $\kappa$  denote the fluid density, heat capacity and thermal conductivity, and are assumed to be  
147 constant. The source term due to the chemical reactions is given by  $S_R = \Delta H_1 R_1 + \Delta H_2 R_2$ , where  $\Delta H_i$  is  
148 the heat release of reaction  $i$ , and  $S_T$  is given in Section 2.4.

149 **2.3. Population balance equation.** We consider the particle formation and growth mechanisms,  
150 and introduce the population balance equation as the means to model them. We assume that we have a  
151 population of particles with different sizes growing at different rates that depend on the chemical species  
152 concentrations and temperature. Let  $dN$  be the number density of particles, that is, the number of particles  
153 per unit volume of gas, at a given spatial location  $\mathbf{x}$ , at a given time  $t$  and with size in the range  $[s, s + ds]$ ,  
154 where we take the diameter of the particle to characterise the particle size. We write  $dN = n(s, \mathbf{x}, t) ds$ ,  
155 which defines the particle size distribution function or number density function  $n(s, \mathbf{x}, t)$  [31].

Parameter	Typical value	Units	Reference
$C_{O_2,0}$	2 – 100	mol/m <sup>3</sup>	Input concentration of O <sub>2</sub> <sup>1</sup>
$C_{SiO,0}$	1	mol/m <sup>3</sup>	Input concentration of SiO <sup>1</sup>
$C_{CO,0}$	1	mol/m <sup>3</sup>	Input concentration of CO <sup>1</sup>
$A_1$	$1.0 \times 10^7$	m <sup>3</sup> /(mol·s)	[18]
$A_2$	$1.80 \times 10^4$	m <sup>3</sup> /(mol·s)	[39]
$T_1$	1713	K	Temperature of the fuel [12]
$T_2$	1073	K	Temperature of the air [12]
$D_{O_2}$	$4.7 \times 10^{-4}$	m <sup>2</sup> /s	[26]
$D_{SiO}$	$3.9 \times 10^{-4}$	m <sup>2</sup> /s	[26]
$D_{SiO_2}$	$3.9 \times 10^{-4}$	m <sup>2</sup> /s	Taken to be the same as $D_{SiO}$
$D_{CO}$	$1.804 \times 10^{-5}$	m <sup>2</sup> /s	[25]
$D_{CO_2}$	$1.429 \times 10^{-5}$	m <sup>2</sup> /s	[25]
$D_p$	$10^{-9}$	m <sup>2</sup> /s	Determined from Stokes-Einstein theory <sup>2</sup>
$c_p$	1005	J/(kg·K)	[18]
$\Delta H_1$	$3.930 \times 10^5$	J/mol	Enthalpy of SiO combustion <sup>3</sup>
$\Delta H_2$	$1.395 \times 10^5$	J/mol	Enthalpy of CO combustion <sup>3</sup>
$E_1$	27196	J/mol	[18]
$E_2$	9974.65	J/mol	[39]
$R$	8.314	J/(mol·K)	Universal gas constant
$\rho_0$	0.3529	kg/m <sup>3</sup>	Density of air <sup>4</sup>
$\kappa$	$5.784 \times 10^{-2}$	W/(m·K)	Thermal conductivity of air <sup>4</sup>
$C_e$	0 – 1	mol/m <sup>3</sup>	Estimated
$M$	$6.008 \times 10^{-2}$	kg/mol	Molar mass of SiO <sub>2</sub>
$m$	$9.96 \times 10^{-26}$	kg	Atomic mass of SiO <sub>2</sub>
$\rho_p$	2196	kg/m <sup>3</sup>	Density of SiO <sub>2</sub>
$s_{\min}$	$2 \times 10^{-8}$	m	Smallest particle seen in experiments <sup>1</sup>
$J_0$	$10^{25}$	1/(m <sup>3</sup> ·s)	[22]
$v_C$	$4.536 \times 10^{-29}$	m <sup>3</sup>	Volume of a molecule of SiO <sub>2</sub>
$\gamma$	$3.20 \times 10^{-2}$	J/m <sup>2</sup>	[12]
$k_B$	$1.3806 \times 10^{-23}$	J/K	Boltzman's constant
$L_V$	$2.1930 \times 10^{10}$	J/m <sup>3</sup>	[21]

Table 1: Typical values of dimensional parameters used in the model. <sup>1</sup> Estimated value obtained from [12]. <sup>2</sup> Stokes-Einstein theory approximates the diffusion coefficient of a particle of radius  $r$  by the relation  $D_p = \frac{k_B T_1}{6\pi\mu r}$ , where  $k_B$  is the Boltzman's constant. <sup>3</sup> Obtained from the software HSC Chemistry. <sup>4</sup> Since air is the dominant component in the fluid. At  $T = 1000$  K and  $P = 1$  atm.

156 The dominant microsilica particle growth mechanisms considered in our model are nucleation and con-  
157 densation, the latter meaning surface growth by the deposition of monomers of SiO<sub>2</sub> on SiO<sub>2</sub> particles.  
158 Letting  $G$  be the growth rate due to condensation, the population balance equation has the form

$$159 \quad (4) \quad \frac{\partial n}{\partial t} - D_p \nabla^2 n + \frac{\partial}{\partial s} \left( G(\mathbf{x}, t) n - D_s \frac{\partial n}{\partial s} \right) = 0.$$

160 The particle-phase or molecular diffusivity,  $D_p$ , is usually negligible for fine particles in turbulent flames  
161 [30, 45]. The main reason is that particles do not diffuse with respect to the gas-phase since their size is  
162 large compared to the gas-phase chemical species. However, the diffusion term may be retained in order to  
163 account for turbulent diffusivity [46]. We can also include diffusion in the size space ( $D_s$ ) which represents  
164 fluctuations around  $G$ . Notice that this diffusion coefficient is dependent on  $G$ , and as an approximation it  
165 can be taken to be proportional to the growth rate [24]. Since the inclusion of  $D_s$  regularises the PDE (4),  
166 it is often added when needed for stability of numerical solutions, though we set  $D_s = 0$  throughout this

167 work. In order to close the model we need to determine the form of the rate expressions for nucleation,  $J$ ,  
 168 which is built into the model via a boundary condition on (4), and for surface growth,  $G$ .

169 **2.3.1. Nucleation rate.** The nucleation rate of particles is included into the model as a boundary  
 170 condition for the particle size coordinate ( $s$ ) in the governing equation (4), by equating it to the “particle  
 171 flux” in at  $s = s_{\min}$  as in [31]:  $n(s_{\min}, t)G(s_{\min}, t) = J$ . We consider homogeneous nucleation as opposed  
 172 to heterogeneous, meaning that the new thermodynamic phase forms spontaneously and randomly rather  
 173 than at nucleation sites on surfaces. The rate at which nucleation of particles occurs is determined by the  
 174 probability of forming the critical nucleus diameter. This is the diameter that maximises the Gibbs free  
 175 energy ( $\Delta\mathcal{G}$ ), which corresponds to where the particle is at equilibrium with the surrounding vapour, and is  
 176 given by  $s_{\min} = 4\gamma v_C / (k_B T \ln S_e)$ , where  $\gamma$ ,  $v_C$ , and  $k_B$  are the surface energy, volume of a  $\text{SiO}_2$  molecule,  
 177 and the Boltzman’s constant, respectively. The quantity  $S_e = C_{\text{SiO}_2} / C_e$  denotes the saturation ratio, with  
 178  $C_e$  being the saturation or equilibrium concentration. Note that in some literature  $S_e$  will be defined as the  
 179 ratio of partial pressures or vapour concentrations [28, 43, 45]. The value of  $C_e$  for  $\text{SiO}_2$  may in general  
 180 depend on a number of atmospheric variables and other considerations, as varying ranges are given for  
 181 different applications [2, 19]. Since a proper value or range of  $C_e$  is not uniquely defined in the literature for  
 182 our problem, we treat  $C_e$  as a parameter which may be varied from zero to one, and determine the sensitivity  
 183 of solutions on this parameter.

184 The value  $s_{\min}$  is the minimum size required for nucleation to occur. The corresponding nucleation rate  
 185 is usually given according to classical nucleation theory [14, 45] as

$$186 \quad (5) \quad J = J_0 \exp\left(-\frac{\Delta\mathcal{G}^*}{k_B T}\right) = J_0 \exp\left(-\frac{16\pi\gamma^3 v_C^2}{3(k_B T)^3 (\ln S_e)^2}\right),$$

187 where we can take the form of the nucleation rate coefficient  $J_0$  from [45], although throughout this paper  
 188 it will be considered to be a constant. Refer to [14, 42] for further details on the derivation of (5).

189 **2.3.2. Growth rate.** Consider a relatively small particle (diameter  $< 1\mu\text{m}$ ) of pure species  $\text{SiO}_2$  in  
 190 air that also contains vapour molecules of  $\text{SiO}_2$ , growing due to vapour condensation. In our case, the mean  
 191 free path of the gas surrounding the particle is large compared to the size of the growing particle itself  
 192 (free-molecule regime) [37], thus classical kinetic theory is applied in order to determine the growth rate.  
 193 We assume the particle to be spherical, and do not take into account any interaction forces between the  
 194 particle and vapour. The collision rate of the gas molecules hitting a unit area in unit time, also called the  
 195 effusion flux, is given by  $\mathcal{F} = N\bar{c}/4$ , where  $N$  is the number concentration of molecules in the gas, and  $\bar{c}$  is  
 196 the mean molecular velocity. The mean velocity is obtained by finding the mean of the Maxwell-Boltzmann  
 197 distribution, and this is  $\bar{c} = \sqrt{8k_B T / (\pi m)}$  where  $k_B$  is the Boltzman’s constant and  $m$  is the atomic mass  
 198 of  $\text{SiO}_2$ . Therefore,  $\mathcal{F} = (C_{\text{SiO}_2} - C_e)\sqrt{8k_B T / (\pi m)}/4$ . The rate of condensation,  $F$ , to the particle surface  
 199 is obtained by multiplying the effusion flux by the surface area of the particle [14], giving

$$200 \quad (6) \quad F = (C_{\text{SiO}_2} - C_e)\sqrt{\frac{k_B T}{2\pi m}}\pi s^2.$$

201 The rate of particle volume growth is then given by multiplying  $F$  by the ratio of  $\text{SiO}_2$  molar mass to density  
 202 so that the dimensions are consistent,

$$203 \quad (7) \quad \frac{dv}{dt} = F\frac{M}{\rho_p} = \sqrt{\frac{k_B T}{2\pi m}}(C_{\text{SiO}_2} - C_e)\pi s^2\frac{M}{\rho_p},$$

204 thus the diameter growth rate is

$$205 \quad (8) \quad \bar{G} = \frac{ds}{dt} = \frac{2M}{\rho_p}\sqrt{\frac{k_B T}{2\pi m}}(C_{\text{SiO}_2} - C_e).$$

206 Since it is well known that microsilica particles do not shrink ( $\bar{G} > 0$ ), in our model we will take

$$207 \quad (9) \quad G = \bar{G}\mathcal{H}(C_{\text{SiO}_2} - C_e)$$

208 as the particle growth rate, where  $\mathcal{H}$  represents the Heaviside function.

209 **2.4. Coupling the particle growth and chemical reaction models.** The particle formation and  
 210 growth model is coupled to the chemical species concentrations and temperature directly via the growth rate  
 211 for condensation,  $G$  and the nucleation rate,  $J$ . These rates depend on the concentration of vapour silicon  
 212 dioxide,  $C_{\text{SiO}_2}$ , predicted by (2d) and on the temperature of the system given by (3).

213 Moreover, in order to account for the material consumed and heat produced due to the formation of the  
 214 particles, we add a sink term  $S_C$  (units  $[\text{mol} \cdot \text{m}^{-3} \cdot \text{s}^{-1}]$ ) in (2d) and a source term  $S_T$  (units  $[\text{J} \cdot \text{m}^{-3} \cdot \text{s}^{-1}]$ )  
 215 in (3). The form of these terms comes from integrating the mass flux through the surface of a spherical  
 216 particle,  $F$  as in (6), times the particle density,  $n$ , over all particle diameters. That is,

$$217 \quad (10) \quad S_C = \int_{s_{\min}}^{\infty} F n ds = \frac{\pi \rho_p}{2 M} G \int_{s_{\min}}^{\infty} s^2 n ds.$$

218 Since mass transfer is the driving mechanism for particle growth, the source term for the energy released due  
 219 to the formation of the particles is proportional to (10). We simply multiply it by the enthalpy of formation  
 220 of the particle,  $\Delta H_p$ , which has physical units  $[\text{J} \cdot \text{mol}^{-1}]$  or equivalently by  $L_V \frac{M}{\rho_p}$ , where  $L_V$  is the specific  
 221 latent heat for condensation with units  $[\text{J} \cdot \text{m}^{-3}]$ . This is,

$$222 \quad (11) \quad S_T = \Delta H_p \int_{s_{\min}}^{\infty} F n ds = \frac{\pi}{2} L_V G \int_{s_{\min}}^{\infty} s^2 n ds.$$

223 **2.5. Moments of the distribution.** In practice, we can decouple the PDE for particle formation (4)  
 224 from the system of ODEs that models the temperature and chemicals by including three extra ODEs for the  
 225 zeroth, first, and second moment of the particle distribution  $n$ , in the following way. First note that the  $k$ th  
 226 moment is given by  $M_k = \int_{s_{\min}}^{\infty} s^k n ds$ , hence the integral part of the expressions derived for  $S_C$  and  $S_T$  in  
 227 the previous section corresponds to  $M_2$ . Now, multiplying the PDE (4) (with  $D_s = 0$ ) by  $s^k$ , for  $k = 0, 1, 2$ ,  
 228 and integrating each case with respect to  $s$ , we obtain the ODEs

$$229 \quad (12) \quad \frac{dM_0}{dt} - D_p \nabla^2 M_0 = J, \quad \frac{dM_1}{dt} - D_p \nabla^2 M_1 = s_{\min} J + G M_0, \quad \frac{dM_2}{dt} - D_p \nabla^2 M_2 = (s_{\min})^2 J + 2G M_1.$$

230 Therefore, we can solve the latter three equations altogether with the concentrations and temperature model,  
 231 and separately from the equation for  $n$  which is slightly more challenging due to the extra dimension. A  
 232 similar approach has been considered elsewhere [28, 43] for solving related population balance models in  
 233 terms of moments.

234 **2.6. Non-dimensional model for a simplified geometry.** From the form of the reaction kinetics,  
 235 the conservation equation for  $\text{N}_2$  decouples from the others, and we do not include it in our model. We  
 236 consider a simplified, one-dimensional geometry given by a cross section of the reaction zone or flame front,  
 237 that is  $z \in (-\infty, \infty)$ , where  $C_{\text{O}_2}$  is initially at maximal concentration as  $z \rightarrow \infty$ , whereas  $C_{\text{SiO}}$  and  $C_{\text{CO}}$  are  
 238 initially at maximal concentration as  $z \rightarrow -\infty$ . Initial data will be prescribed based on the desired initial  
 239 configuration, with either well-mixed or spatially partitioned initial profiles for the initial concentrations of  
 240 chemicals and temperature. We shall assume a zero initial profile for the particle distribution as well as for  
 241 the moments; there will be no particles already in the system at the initial time. Thus, the initial conditions  
 242 can be written as  $C_X = C_{X,\text{initial}}(z)$ ,  $T = T_{\text{initial}}(z)$ ,  $n = M_0 = M_1 = M_2 = 0$  at  $t = 0$ , where the form of  
 243 the functions will be discussed later. We also have a boundary condition for  $n$ ,  $Gn = J$  at  $s = s_{\min}$ , with  
 244 the dimensional particle growth,  $G$ , and nucleation,  $J$ , rates given by (9) and (5), respectively.

245 We non-dimensionalise the equations previously defined by scaling the variables in the following way:  
 246  $T = (T_1 - T_2)\tilde{T} + T_2$ , where  $T_1$  is the temperature of the fuel as it leaves the charge surface and  $T_2$  is the  
 247 temperature of the air coming from outside the furnace (in practice  $T_2 < T_1$ ),  $C_X = C_{X,0}\tilde{C}_X$ , where  $C_{X,0}$   
 248 represents the input concentration of the reactant  $X$  while for the products we take  $C_{\text{SiO}_2,0} = C_{\text{SiO},0}$  and  
 249  $C_{\text{CO}_2,0} = C_{\text{CO},0}$ ,  $t = t_0\tilde{t}$ ,  $z = z_0\tilde{z}$ ,  $s = s_0\tilde{s}$ ,  $n = n_0\tilde{n}$ , and  $M_i = m_i\tilde{M}_i$  for  $i = 0, 1, 2$ . We choose the timescale  
 250 with the dominant reaction kinetics and the spatial scale is taken with the dominant diffusion  $D_{\text{O}_2}$ , namely

$$251 \quad (13) \quad t_0 = \frac{1}{2A_1 C_{\text{O}_2,0}} \exp\left(\frac{E_1}{RT_1}\right), \quad z_0 = \sqrt{D_{\text{O}_2} t_0} = \sqrt{\frac{D_{\text{O}_2}}{2A_1 C_{\text{O}_2,0}} \exp\left(\frac{E_1}{2RT_1}\right)}.$$

Dimensionless parameter	Relation with dimensional parameters	Typical value
$d_{\text{SiO}}$	$\frac{D_{\text{SiO}}}{D_{\text{O}_2}}$	0.8298
$d_{\text{SiO}_2}$	$\frac{D_{\text{SiO}_2}}{D_{\text{O}_2}}$	0.8298
$d_{\text{CO}}$	$\frac{D_{\text{CO}}}{D_{\text{O}_2}}$	$3.829 \times 10^{-2}$
$d_{\text{CO}_2}$	$\frac{D_{\text{CO}_2}}{D_{\text{O}_2}}$	$3.040 \times 10^{-2}$
$Le$	$\frac{\kappa}{\rho_0 c_p D_{\text{O}_2}}$	0.3470
$a$	$\frac{C_{\text{SiO},0}}{C_{\text{O}_2,0}}$	$10^{-3} - 0.2$
$\varepsilon$	$\frac{A_2}{A_1} \exp\left(\frac{E_1 - E_2}{RT_1}\right)$	$6.031 \times 10^{-3}$
$h_1$	$\frac{C_{\text{SiO},0} \Delta H_1}{2(T_1 - T_2) \rho_0 c_p}$	0.8591
$h_2$	$\frac{C_{\text{CO},0} \Delta H_2}{2(T_1 - T_2) \rho_0 c_p}$	0.3073
$\alpha_1$	$\exp\left(-\frac{E_1}{R} \left(\frac{1}{T_2} - \frac{1}{T_1}\right)\right)$	0.32
$\alpha_2$	$\exp\left(-\frac{E_2}{R} \left(\frac{1}{T_2} - \frac{1}{T_1}\right)\right)$	0.659
$\zeta_1$	$\frac{\pi \rho_p J_0 (s_{\min})^3}{4M A_1 C_{\text{O}_2,0} C_{\text{SiO}_2,0}} \exp\left(\frac{E_1}{RT_1}\right)$	$3.875 \times 10^{-2}$
$\zeta_2$	$\frac{\pi L_V J_0 (s_{\min})^3}{4\rho_0 c_p A_1 C_{\text{O}_2,0} (T_1 - T_2)} \exp\left(\frac{E_1}{RT_1}\right)$	0.1024
$d_p$	$\frac{D_p}{D_{\text{O}_2}}$	$2.128 \times 10^{-6}$
$T^*$	$\frac{T_2}{T_1 - T_2}$	1.677
$G^*$	$\frac{M C_{\text{SiO}_2,0} \sqrt{T_1 - T_2}}{\rho_p A_1 C_{\text{O}_2,0} s_{\min}} \sqrt{\frac{k_B}{2\pi m}} \exp\left(\frac{E_1}{RT_1}\right)$	$4.39 \times 10^{-2}$
$J^*$	$\frac{J_0 \rho_p}{M \times 10^{23} C_{\text{SiO}_2,0} \sqrt{T_1 - T_2}} \sqrt{\frac{\pi m}{2k_B}}$	$1.538 \times 10^4$
$C_{\text{sat}}$	$\frac{C_\varepsilon}{C_{\text{SiO}_2,0}}$	0 - 1
$\lambda$	$\frac{16\pi\gamma^3 v_C^2}{3k_B^3 T_2^3}$	0.3474

Table 2: Definitions and typical values for non-dimensional parameters used in the model. We treat  $a$  and  $C_{\text{sat}}$  as control parameters, whereas the other parameters are determined from values in Table 1.

252 Additionally, we scale the particle diameter with the critical diameter for nucleation,  $s_0 = s_{\min}$ , the num-  
253 ber density function with the ratio between nucleation and growth rate coefficients,  $n_0 = J_0/G_0$  where  
254  $G_0 = 2MC_{\text{SiO}_2,0} \sqrt{k_B(T_1 - T_2)}/(2\pi m)/\rho_p = 6.5 \times 10^{-3}$ , and the moments with a combination of the latter  
255 two scalings,  $m_i = n_0 s_0^{i+1}$ ,  $i = 0, 1, 2$ . A full list of dimensionless parameter groups is given in Table 2.

256 With these scalings and dropping the over tilde notation, the dimensionless equations read

257 (14a) 
$$\frac{\partial C_{\text{O}_2}}{\partial t} - \frac{\partial^2 C_{\text{O}_2}}{\partial z^2} = -\frac{a}{2} (f_1(T) C_{\text{O}_2} C_{\text{SiO}} + \varepsilon f_2(T) C_{\text{O}_2} C_{\text{CO}}),$$

258 (14b) 
$$\frac{\partial C_{\text{SiO}}}{\partial t} - d_{\text{SiO}} \frac{\partial^2 C_{\text{SiO}}}{\partial z^2} = -f_1(T) C_{\text{O}_2} C_{\text{SiO}},$$

259 (14c) 
$$\frac{\partial C_{\text{SiO}_2}}{\partial t} - d_{\text{SiO}_2} \frac{\partial^2 C_{\text{SiO}_2}}{\partial z^2} = f_1(T) C_{\text{O}_2} C_{\text{SiO}} - \zeta_1 G(z, t) M_2,$$

260 (14d) 
$$\frac{\partial C_{\text{CO}}}{\partial t} - d_{\text{CO}} \frac{\partial^2 C_{\text{CO}}}{\partial z^2} = -\varepsilon f_2(T) C_{\text{O}_2} C_{\text{CO}},$$

261 (14e) 
$$\frac{\partial C_{\text{CO}_2}}{\partial t} - d_{\text{CO}_2} \frac{\partial^2 C_{\text{CO}_2}}{\partial z^2} = \varepsilon f_2(T) C_{\text{O}_2} C_{\text{CO}},$$

262 (14f) 
$$\frac{\partial T}{\partial t} - Le \frac{\partial^2 T}{\partial z^2} = h_1 f_1(T) C_{\text{O}_2} C_{\text{SiO}} + \varepsilon h_2 f_2(T) C_{\text{O}_2} C_{\text{CO}} + \zeta_2 G(z, t) M_2,$$

263

$$264 \quad (14g) \quad \frac{\partial M_0}{\partial t} - d_p \frac{\partial^2 M_0}{\partial z^2} = G^* J(z, t),$$

$$265 \quad (14h) \quad \frac{\partial M_1}{\partial t} - d_p \frac{\partial^2 M_1}{\partial z^2} = G^* J(z, t) + G^* G(z, t) M_0,$$

$$266 \quad (14i) \quad \frac{\partial M_2}{\partial t} - d_p \frac{\partial^2 M_2}{\partial z^2} = G^* J(z, t) + 2G^* G(z, t) M_1,$$

267 for  $-\infty < z < \infty$ ,  $t > 0$ . The dimensionless Arrhenius terms in the reaction rates have the form

$$268 \quad (15) \quad f_j(T) = \exp\left(-\frac{E_j}{R} \left(\frac{1}{(T_1 - T_2)T + T_2} - \frac{1}{T_1}\right)\right), \quad j = 1, 2,$$

269 and the non-dimensional particle growth and nucleation rates are given by

$$270 \quad (16) \quad G = \sqrt{T + T^*} (C_{\text{SiO}_2} - C_{\text{sat}}) \mathcal{H}(C_{\text{SiO}_2} - C_{\text{sat}}) \quad \text{and} \quad J = \exp\left(-\frac{\lambda}{\left(\frac{T}{T^*} + 1\right)^3 \ln^2\left(\frac{C_{\text{SiO}_2}}{C_{\text{sat}}}\right)}\right),$$

271 respectively. The dimensionless initial conditions are the following:

$$272 \quad (17) \quad C_X = \frac{C_{X,\text{initial}}(z)}{C_{X,0}}, \quad T = \frac{T_{\text{initial}}(z) - T_2}{T_1 - T_2}, \quad M_0 = M_1 = M_2 = 0 \quad \text{at} \quad t = 0.$$

273 In the non-dimensionalisation we assumed that the input value of all the chemical species is the same  
 274 except for the oxygen, that is  $C_{\text{SiO},0} = C_{\text{SiO}_2,0} = C_{\text{CO},0} = C_{\text{CO}_2,0}$ . Thus,  $a$  represents the ratio of the  
 275 maximum concentration of these species to the maximum concentration of oxygen,  $\varepsilon$  is the ratio between  
 276 the reaction rates, and  $h_1$  and  $h_2$  measure the balance between the reactant concentration needed to give off  
 277 heat and the role of the respective reaction on generating heat.

278 Finally, the particle formation and growth problem in non-dimensional form reads

$$279 \quad (18a) \quad \frac{\partial n}{\partial t} - d_p \frac{\partial^2 n}{\partial z^2} = -G^* G(z, t) \frac{\partial n}{\partial s} \quad \text{for} \quad -\infty < z < \infty, \quad s > 1, \quad t > 0,$$

280

$$281 \quad (18b) \quad n = 0 \quad \text{at} \quad t = 0, \quad \text{and} \quad Gn = J \quad \text{at} \quad s = 1.$$

282 **3. The case of well-mixed chemical species.** We first consider the case where the chemical species  
 283 are well-mixed, with uniform initial concentrations and temperature for all  $z \in \mathbb{R}$ , so that the concentrations  
 284 and temperature are independent of  $z$  for all  $t \geq 0$ . This limit is best viewed as a simplification of the spatial  
 285 structure taken in order to better qualitatively understand the dynamics taking place within the interior of  
 286 the reaction zone, whereas in the next section we will more accurately depict the macroscopic scale structure  
 287 of the reaction zone between two larger non-reacting regions. Under this assumption, equations (14a)-(14i)  
 288 reduce to the system

$$289 \quad (19a) \quad \frac{dC_{\text{O}_2}}{dt} = -\frac{a}{2} (f_1(T)C_{\text{O}_2}C_{\text{SiO}} + \varepsilon f_2(T)C_{\text{O}_2}C_{\text{CO}}),$$

$$290 \quad (19b) \quad \frac{dC_{\text{SiO}}}{dt} = -f_1(T)C_{\text{O}_2}C_{\text{SiO}},$$

$$291 \quad (19c) \quad \frac{dC_{\text{SiO}_2}}{dt} = f_1(T)C_{\text{O}_2}C_{\text{SiO}} - \zeta_1 G(t)M_2,$$

$$292 \quad (19d) \quad \frac{dC_{\text{CO}}}{dt} = -\varepsilon f_2(T)C_{\text{O}_2}C_{\text{CO}},$$

$$293 \quad (19e) \quad \frac{dC_{\text{CO}_2}}{dt} = \varepsilon f_2(T)C_{\text{O}_2}C_{\text{CO}},$$

$$294 \quad (19f) \quad \frac{dT}{dt} = h_1 f_1(T)C_{\text{O}_2}C_{\text{SiO}} + \varepsilon h_2 f_2(T)C_{\text{O}_2}C_{\text{CO}} + \zeta_2 G(t)M_2,$$

$$295 \quad (19g) \quad \frac{dM_0}{dt} = G^* J(t), \quad \frac{dM_1}{dt} = G^* J(t) + G^* G(t)M_0, \quad \frac{dM_2}{dt} = G^* J(t) + 2G^* G(t)M_1,$$

296 for  $t > 0$ , while the initial conditions become

$$297 \quad (20a) \quad C_{O_2} = C_{SiO} = C_{CO} = T = 1, \quad C_{SiO_2} = C_{CO_2} = M_0 = M_1 = M_2 = 0 \quad \text{at} \quad t = 0,$$

298 The particle formation and growth system (18) reduces to

$$299 \quad (21a) \quad \frac{\partial n}{\partial t} = -G^*G(t)\frac{\partial n}{\partial s} \quad \text{for} \quad s > 1, \quad t > 1,$$

$$300 \quad (21b) \quad n = 0 \quad \text{at} \quad t = 0, \quad \text{and} \quad Gn = J \quad \text{at} \quad s = 1.$$

301 **3.1. Analytical solution to the chemical - temperature problem.** For analytical tractability we  
 302 shall set  $\zeta_1 = \zeta_2 = 0$ . Several conservation laws for the concentrations and temperature are apparent and we  
 303 no longer need to solve for the moments of the distribution since they decouple from the system. Combining  
 304 (19d) and (19e), and (19b) and (19c) we obtain

$$305 \quad (22a) \quad C_{CO_2} = 1 - C_{CO}, \quad C_{SiO_2} = 1 - C_{SiO},$$

307 respectively. Now using (19a), (19b), and (19d), we find

$$308 \quad (22b) \quad C_{O_2} = 1 - \frac{a}{2}[(1 - C_{SiO}) + (1 - C_{CO})],$$

310 and finally combining (19b), (19d), and (19f), we obtain

$$311 \quad (22c) \quad T = 1 + h_1(1 - C_{SiO}) + h_2(1 - C_{CO}).$$

313 Making use of these conservation laws, we eliminate  $C_{O_2}$ ,  $C_{SiO_2}$ ,  $C_{CO_2}$ , and  $T$ , obtaining the system

$$314 \quad (23a) \quad \frac{dC_{SiO}}{dt} = -f_1(1 + h_1(1 - C_{SiO}) + h_2(1 - C_{CO})) \left(1 - \frac{a}{2}[(1 - C_{SiO}) + (1 - C_{CO})]\right) C_{SiO},$$

$$315 \quad (23b) \quad \frac{dC_{CO}}{dt} = -\varepsilon f_2(1 + h_1(1 - C_{SiO}) + h_2(1 - C_{CO})) \left(1 - \frac{a}{2}[(1 - C_{SiO}) + (1 - C_{CO})]\right) C_{CO},$$

316 subject to  $C_{SiO}(0) = C_{CO}(0) = 1$ .

317 **3.1.1. Multiple timescale analysis.** In order to understand the dynamics from (23), we first make  
 318 several observations. First, for any  $C_{SiO}(t), C_{CO}(t) \in (0, 1]$ , we have that

$$319 \quad (24a) \quad 0 < f_1(1 + h_1(1 - C_{SiO}) + h_2(1 - C_{CO})) \left(1 - \frac{a}{2}[(1 - C_{SiO}) + (1 - C_{CO})]\right) C_{SiO} \leq f_1(1 + h_1 + h_2),$$

$$320 \quad (24b) \quad 0 < f_2(1 + h_1(1 - C_{SiO}) + h_2(1 - C_{CO})) \left(1 - \frac{a}{2}[(1 - C_{SiO}) + (1 - C_{CO})]\right) C_{CO} \leq f_2(1 + h_1 + h_2),$$

321 thus  $C_{SiO}(t)$  and  $C_{CO}(t)$  are monotone decreasing from 1 to 0. Second, since  $0 < \varepsilon \ll 1$ , the dynamics of  
 322 (23b) are on a slower timescale than those of (23a). Introducing the slow timescale  $\tau = \varepsilon t$ , and writing  
 323  $C_{CO} = C_{CO}(\tau)$ , we have

$$324 \quad (25a) \quad \frac{dC_{SiO}}{dt} = -f_1(1 + h_1(1 - C_{SiO}(t)) + h_2(1 - C_{CO}(\varepsilon t))) \left(1 - \frac{a}{2}[(1 - C_{SiO}(t)) + (1 - C_{CO}(\varepsilon t))]\right) C_{SiO}(t),$$

$$325 \quad (25b) \quad \frac{dC_{CO}}{d\tau} = -f_2(1 + h_1(1 - C_{SiO}(\tau/\varepsilon)) + h_2(1 - C_{CO}(\tau))) \left(1 - \frac{a}{2}[(1 - C_{SiO}(\tau/\varepsilon)) + (1 - C_{CO}(\tau))]\right) C_{CO}(\tau).$$

327 In (25a),  $C_{CO}(\varepsilon t)$  is slowly varying and can be treated as a constant at lowest order, relative to the  
 328 timescale on which  $C_{SiO}(t)$  varies. Similarly, in (25b),  $C_{SiO}(\tau/\varepsilon)$  is rapidly varying and nears its equilibrium  
 329 value before  $C_{CO}(\tau)$  responds. Therefore, we approximate (25) by approximating  $C_{CO}(\varepsilon t) = 1$  on the  
 330 timescale  $t$  and  $C_{SiO}(\tau/\varepsilon) = 0$  on the timescale  $\tau$ . We obtain

$$331 \quad (26a) \quad \frac{dC_{SiO}}{dt} = -f_1(1 + h_1(1 - C_{SiO}(t))) \left(1 - \frac{a}{2}(1 - C_{SiO}(t))\right) C_{SiO}(t),$$

$$332 \quad (26b) \quad \frac{dC_{CO}}{d\tau} = -f_2(1 + h_1 + h_2(1 - C_{CO}(\tau))) \left(1 - \frac{a}{2}[1 + (1 - C_{CO}(\tau))]\right) C_{CO}(\tau).$$

333

334 Solving (26) by quadrature, we obtain the implicit relations

$$335 \quad (27) \quad \int_{C_{\text{SiO}}}^1 \frac{d\xi}{f_1(1+h_1(1-\xi))(1-\frac{a}{2}(1-\xi))\xi} = t, \quad \int_{C_{\text{CO}}}^1 \frac{d\xi}{f_2(1+h_1+h_2(1-\xi))(1-\frac{a}{2}(2-\xi))\xi} = \tau,$$

336 where it is clear that  $C_{\text{SiO}}, C_{\text{CO}} \rightarrow 0$  as  $t \rightarrow \infty$ , as expected. In order to obtain more explicit representations  
337 of the solutions, we make further assumptions.

338 **3.1.2. Approximating the Arrhenius terms.** We shall at times find it convenient to approximate  
339 the Arrhenius terms in the reaction kinetics (15) with linear approximations,  $f_j(T) \approx F_j(T)$ , where

$$340 \quad (28) \quad F_j(T) = \alpha_j + (1 - \alpha_j)T \quad \text{with} \quad \alpha_j = \exp\left(-\frac{E_j}{R}\left(\frac{1}{T_2} - \frac{1}{T_1}\right)\right).$$

341 The error estimate of this approximation based on the initial data for  $T$  is  $\max_{T \in [0,1]} \frac{|f_1(T) - F_1(T)|}{f_1(T)} = 0.031$   
342 and  $\max_{T \in [0,1]} \frac{|f_2(T) - F_2(T)|}{f_2(T)} = 0.027$  for parameter values in Table 2. Hence, the maximal relative error for  
343  $0 \leq T \leq 1$  is around 3%. Later on we will see that at certain spatial locations and times the temperature  
344 can go up to 2 approximately. In this case, the maximal relative error for  $0 \leq T \leq 2$  is around 5% for  $F_1$  and  
345 8% for  $F_2$ . We conclude that the error of this approximation is low enough over the range of temperatures  
346 considered so that the qualitative behaviour of the solutions is unaltered. Notice that the temperature will  
347 only go beyond 2 when we solve the full problem numerically, however there is no need for an approximation  
348 of the Arrhenius terms in this case.

349 **3.1.3. Small  $a$  asymptotics.** Making use of the approximation (28), we write

$$350 \quad (29a) \quad \frac{dC_{\text{SiO}}}{dt} = -(\alpha_1 + (1 - \alpha_1)[1 + h_1(1 - C_{\text{SiO}})]) \left(1 - \frac{a}{2}(1 - C_{\text{SiO}})\right) C_{\text{SiO}},$$

$$351 \quad (29b) \quad \frac{dC_{\text{CO}}}{d\tau} = -(\alpha_2 + (1 - \alpha_2)[1 + h_1 + h_2(1 - C_{\text{CO}})]) \left(1 - \frac{a}{2}[1 + (1 - C_{\text{CO}})]\right) C_{\text{CO}}.$$

353 Recall that  $0 < a \leq 0.2$ . We therefore treat  $a$  as a small parameter,  $a \ll 1$ , and at lowest order in  $a$ , the  
354 ODEs (29) become quadratic rather than cubic. Solving these lowest order equations subject to  $C_{\text{SiO}}(0) = 1$   
355 and  $C_{\text{CO}}(0) = 1$ , respectively, we find that the asymptotic solutions in the small  $a$  limit are

$$356 \quad (30a) \quad C_{\text{SiO}}(t) = \frac{1 + h_1(1 - \alpha_1)}{\exp([1 + h_1(1 - \alpha_1)]t) + h_1(1 - \alpha_1)} + \mathcal{O}(a),$$

$$357 \quad (30b) \quad C_{\text{CO}}(t) = \frac{1 + (h_1 + h_2)(1 - \alpha_2)}{(1 + h_1(1 - \alpha_2)) \exp([1 + (h_1 + h_2)(1 - \alpha_2)]\varepsilon t) + h_2(1 - \alpha_2)} + \mathcal{O}(a).$$

359 Asymptotic solutions for all remaining quantities can be obtained from (30) and the earlier mentioned  
360 conservation laws (22a)-(22c). We plot the approximate solutions in Figure 3 for one small value of  $a$  (left)  
361 and the upper bound  $a = 0.2$  (right). We see that since  $C_{\text{CO}}$  and  $C_{\text{CO}_2}$  evolve on a slower timescale than  
362 the rest of the chemical concentrations, the second reaction has not happened yet while the first one finishes  
363 within the selected timescale. When comparing the analytical approximations (solid line) to the numerical  
364 simulations (dashed line) we find good agreement, even for relatively large values of  $a$ , so the analytical  
365 solution retains validity in the physically relevant parameter regime.

366 **3.2. Analytical solution of the particle density equation.** We find an analytical solution for the  
367 particle density function by solving the problem (21) in terms of the growth rate  $G$  and nucleation rate  $J$   
368 as given in (16), which depend on  $C_{\text{SiO}_2}$  and  $T$ . First, we define  $t_{\min}$  to be the minimal value of  $t$  such that  
369  $C_{\text{SiO}_2}(t_{\min}) = C_{\text{sat}}$ . Noting that  $1 - C_{\text{SiO}}(t_{\min}) = C_{\text{SiO}_2}(t_{\min}) = C_{\text{sat}}$ , and employing the asymptotic solution  
370 (30a), we find

$$371 \quad (31) \quad t_{\min} = \frac{1}{1 + h_1(1 - \alpha_1)} \log\left(\frac{1 + h_1(1 - \alpha_1)C_{\text{sat}}}{1 - C_{\text{sat}}}\right) + \mathcal{O}(a)$$

372 as  $a \rightarrow 0$ . In the case where  $t \leq t_{\min}$ , equation (21a) reduces to  $\partial n / \partial s = 0$  for  $s > 1$ , with  $n = 0$  at  $t = 0$ ,  
373 hence the solution is  $n = 0$ . This makes sense since no particles are formed before the concentration reaches

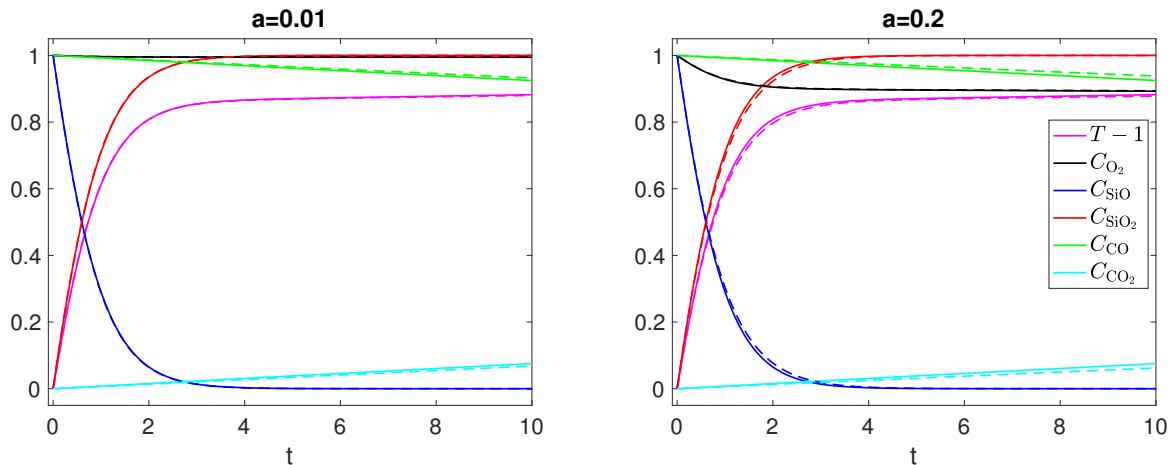


Fig. 3: Dimensionless chemical concentrations and temperature as indicated in the legend from solving the problem (19)-(20) numerically (dashed line) and analytically (solid line) assuming  $\zeta_1 = \zeta_2 = 0$ . We compare the solutions for  $a = 0.01$  (left) and  $a = 0.2$  (right). We fix  $C_{\text{sat}} = 0.1$ , with other parameters taking values listed in Table 2.

374 saturation. For the second case where  $t > t_{\text{min}}$ , we use the method of characteristics to obtain a parametric  
 375 solution for  $n$ . For characteristics emanating from  $t = t_{\text{min}}$ , given by

$$376 \quad (32) \quad s = s_1 + G^* \int_{t_{\text{min}}}^t G(\tau) d\tau$$

377 with  $s_1 > 1$ , the solution is always  $n = 0$ . For characteristic curves emerging from  $s = 1$ , given implicitly by

$$378 \quad (33) \quad s = 1 + G^* \int_{t_1}^t G(\tau) d\tau$$

379 with  $t_1 > t_{\text{min}}$ , the solution is

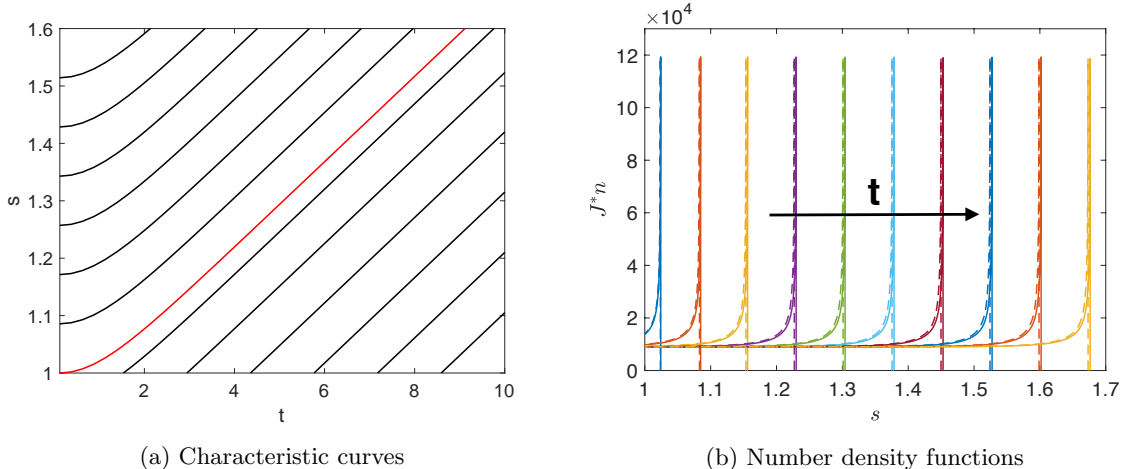
$$380 \quad (34) \quad n = \frac{J(t_1)}{G(t_1)}.$$

381 In Figure 4a, we plot the characteristic curves, with the red curve corresponding to the dividing characteristic  
 382 that bounds both regions and is given implicitly by

$$383 \quad (35) \quad s^*(t) = 1 + G^* \int_{t_{\text{min}}}^t G(\tau) d\tau.$$

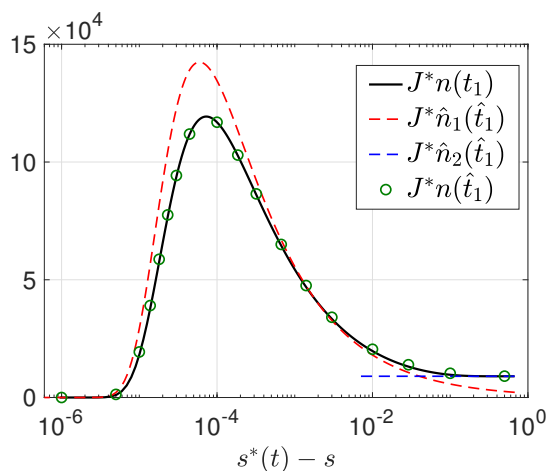
384 In the region above this curve the solution is  $n = 0$ , whereas below it is given by (34). In Figure 4b, we show  
 385 the solution for  $n$  given by (33) and (34), where we take  $C_{\text{SiO}_2}$  and  $T$  from both the analytical approximations  
 386 and numerical simulations in the previous section with  $a = 0.2$ . The main difference we see between the  
 387 particle density functions obtained using both approximations is the position of the peaks. This is due to  
 388 the small shift in the  $C_{\text{SiO}_2}$  curves in Figure 3; the concentration will reach the saturation point at a slightly  
 389 different time  $t_{\text{min}}$ . Here, we have chosen  $C'_{\text{sat}} = 0.1$ , thus  $t_{\text{min}} = 0.106$  in the numerics (dashed line) and  
 390  $t_{\text{min}} = 0.103$  in the analytics (solid line). Since in the latter case the particles start growing at an earlier  
 391 time, they grow to be larger.

392 In Figure 4b, we see that as time evolves the peaks move to the right, meaning that the particles grow.  
 393 With respect to the shape of  $n$  for a specific time, we find a uniform distribution at smaller sizes, and a  
 394 peak around the largest sizes. The largest number of particles are of the largest sizes, and these particles  
 395 originated very close to  $t = t_{\text{min}}$ , with their change in diameter over time (the position of the peaks)



(a) Characteristic curves

(b) Number density functions



(c) Semi-log plot for the number density function (black) and asymptotic approximations (dashed lines and circles).

Fig. 4: (a) Characteristic curves corresponding to problem (21) where the red line is the limiting curve given by (35). In (b) we show the dimensionless number density function of particles for different values of  $t$  from 1 to 10 with an increment of 1. The curves are obtained from solving the problem (19a)-(19f), with  $\zeta_1, \zeta_2 = 0$ , numerically (dashed line) and analytically (solid line) for  $a = 0.2$  and using the formulae (33) and (34) for  $n$ . In (c) we provide a semi-log plot for the number density functions from (b) (black solid line), for  $n$  with asymptotic approximations for the characteristics (40) (green circles), and for the asymptotic approximations of the peak (41) (red dashed line) and uniform (44) (blue dashed line) parts of the distribution. The legend indicates the meaning of each curve. We have chosen  $C_{\text{sat}} = 0.1$  and have scaled  $n$  with the dimensionless parameter  $J^* = J_0/(10^{23}G_0)$  from Table 2.

396 determined approximately by the characteristic  $s^*(t)$  highlighted in red in Figure 4a. We show the solution  
 397 corresponding to the last peak in Figure 4b ( $t = 10$ ) in a semi-log plot in Figure 4c with a black solid curve.

398 In order to better understand the parameter dependence of the peak, we consider an asymptotic analysis  
 399 near the red characteristic. We use the approximated solutions for  $C_{\text{SiO}_2}$  and  $T$  from Section 3.1, neglecting  
 400 terms which evolve on the slow timescale  $\tau = \epsilon t$  and setting  $C_{\text{CO}}(t) \approx 1$  for  $t \ll \epsilon^{-1}$ . We also neglect  
 401  $\mathcal{O}(a)$  terms. From Figure 4c (black solid line), there are two timescales to consider. The first timescale  
 402 corresponds to  $0 < t - t_{\text{min}} \ll 1$ , for which  $0 < s^*(t) - s \ll 1$ , and we have the observed peak in Figures  
 403 4b and 4c. For  $t - t_{\text{min}} \gg 1$ , we have the flat region of uniform distribution away from the peak, which  
 404 corresponds to  $C_{\text{SiO}_2} \sim 1$  and  $T(t) \sim 1 + h_1$ , as seen in Figure 3. The reaction leading to particle growth  
 405 happens before the very large timescales on which  $C_{\text{CO}}$  will play a role, so we consider  $1 \ll t - t_{\text{min}} \ll \epsilon^{-1}$

406 for our second timescale.

407 **3.2.1. The small timescale**,  $0 < t - t_{\min} \ll 1$ . Expanding the analytical solutions for  $C_{\text{SiO}_2}$  and  $T$ ,  
 408 (22a) and (22c) with (30), found in Section 3.1 in  $t - t_{\min}$ , we write

409 (36a) 
$$C_{\text{SiO}_2}(t) = C_{\text{sat}} + (1 - C_{\text{sat}})(1 + h_1(1 - \alpha_1)C_{\text{sat}})(t - t_{\min}) + \mathcal{O}\left((t - t_{\min})^2\right),$$

410 (36b) 
$$T(t) = 1 + h_1 C_{\text{sat}} + h_1(1 - C_{\text{sat}})(1 + h_1(1 - \alpha_1)C_{\text{sat}})(t - t_{\min}) + \mathcal{O}\left((t - t_{\min})^2\right).$$
  
 411

412 These approximations allow us to approximate the characteristic curves (33) by the formula

413 (37) 
$$s = 1 + \frac{G^*}{2} \sqrt{T^* + 1 + h_1 C_{\text{sat}}(1 - C_{\text{sat}})(1 + h_1(1 - \alpha_1)C_{\text{sat}})} \left\{ (t - t_{\min})^2 - (t_1 - t_{\min})^2 \right\},$$

where we have used

$$\sqrt{T^* + 1 + h_1 C_{\text{sat}} + h_1(1 - C_{\text{sat}})(1 + h_1(1 - \alpha_1)C_{\text{sat}})}(t - t_{\min}) \approx \sqrt{T^* + 1 + h_1 C_{\text{sat}}}.$$

414 We find

415 (38) 
$$t_1 = t_{\min} + \sqrt{(t - t_{\min})^2 - \frac{s - 1}{\frac{G^*}{2} \sqrt{T^* + 1 + h_1 C_{\text{sat}}(1 - C_{\text{sat}})(1 + h_1(1 - \alpha_1)C_{\text{sat}})}},$$

416 and similarly for (35), we obtain

417 (39) 
$$s^*(t) = 1 + \frac{G^*}{2} \sqrt{T^* + 1 + h_1 C_{\text{sat}}(1 - C_{\text{sat}})(1 + h_1(1 - \alpha_1)C_{\text{sat}})}(t - t_{\min})^2.$$

418 Therefore, we may write

419 (40) 
$$t_1 \approx \hat{t}_1 = t_{\min} + \sqrt{\frac{s^*(t) - s}{\frac{G^*}{2} \sqrt{T^* + 1 + h_1 C_{\text{sat}}(1 - C_{\text{sat}})(1 + h_1(1 - \alpha_1)C_{\text{sat}})}},$$

420 where it will be convenient to define the moving coordinate  $S = s^*(t) - s$ . We remark that the small  $t - t_{\min}$   
 421 regime corresponds to the small  $S$  regime. We evaluate the exact solution  $n(t_1)$  at the explicit approximation  
 422 of  $t_1$  as given by (40) and plot it in Figure 4c with green circles to find that it matches the real solution  
 423 (black solid line) everywhere. As such, the approximate characteristic curves result in nearly the same exact  
 424 solution (plotted numerically), and do not introduce significant error.

425 From the implicit form of the exact solution,  $n(s, t) = J(t_1)/G(t_1)$ , we now use the approximation of  $t_1$   
 426 to construct an approximation  $\hat{n}_1$  to  $n$  which is explicit in the variables. We find

427 (41a) 
$$n = \frac{\exp\left\{-\lambda\left(\frac{T(t_1)}{T^*} + 1\right)^{-3}\left[\ln\left(\frac{C_{\text{SiO}_2}(t_1)}{C_{\text{sat}}}\right)\right]^{-2}\right\}}{\sqrt{T^* + T(t_1)}(C_{\text{SiO}_2}(t_1) - C_{\text{sat}})} \approx \hat{n}_1(S) = \frac{\Gamma}{\sqrt{S}} \exp\left(-\frac{\Lambda}{S}\right),$$
  
 428  
 429

430 (41b) 
$$\Gamma = \sqrt{\frac{G^*}{2\sqrt{T^* + 1 + h_1 C_{\text{sat}}(1 - C_{\text{sat}})(1 + h_1(1 - \alpha_1)C_{\text{sat}})}},$$

431 (41c) 
$$\Lambda = \frac{\lambda G^* T^{*3} C_{\text{sat}}^2}{2(T^* + 1 + h_1 C_{\text{sat}})^{5/2}(1 - C_{\text{sat}})(1 + h_1(1 - \alpha_1)C_{\text{sat}})}.$$
  
 432

433 Here  $\Gamma$  and  $\Lambda$  are constants which depend on model parameters. From (41a), the position and height of  
 434 the peak are given by  $s_p = s^*(t) - 2\Lambda$  and  $\hat{n}_1(s_p) = \Gamma \exp(-1/2)/\sqrt{2\Lambda}$ , respectively. Note that the position  
 435 is time-dependent. Using Table 2 and  $C_{\text{sat}} = 0.1$ , we find  $\Gamma = 0.117$  and  $\Lambda = 3.268 \times 10^{-5}$ . We plot  
 436 the approximation (41a) with a red dashed curve in Figure 4c and find that the width of the peak is well  
 437 represented, as is the rate of change on each side of the peak, while the height of the peak is slightly  
 438 overestimated (and would, in principle, be improved by the inclusion of higher order terms).

439 **3.2.2. The larger timescale**,  $1 \ll t - t_{\min} \ll \varepsilon^{-1}$ . On the timescale  $1 \ll t - t_{\min} \ll \varepsilon^{-1}$ , we  
 440 have  $C_{\text{SiO}_2}(t) = 1 - \mathcal{O}(\exp\{-(1 + h_1(1 - \alpha_1))t\})$  and  $T(t) = 1 + h_1 - \mathcal{O}(\exp\{-(1 + h_1(1 - \alpha_1))t\})$ , and we  
 441 approximate  $C_{\text{SiO}_2}(t) \approx 1$  and  $T(t) \approx 1 + h_1$ . Similar to the above, we find

$$442 \quad (42) \quad s = 1 + G^* \int_{t_1}^t \sqrt{T^* + T(\tau)} (C_{\text{SiO}_2}(\tau) - C_{\text{sat}}) d\tau = 1 + G^* \sqrt{T^* + 1 + h_1} (1 - C_{\text{sat}}) (t - t_1),$$

$$443 \quad (43) \quad s^*(t) = 1 + G^* \sqrt{T^* + 1 + h_1} (1 - C_{\text{sat}}) (t - t_{\min}).$$

445 From this we note that the characteristic curves become lines once  $S = \mathcal{O}(1)$ , consistent with what is  
 446 observed in Figure 4a once  $s$  is an  $\mathcal{O}(1)$  distance away from the curve  $s^*(t)$  (shown in red). Manipulating  
 447 these equations, we obtain

$$448 \quad (44) \quad t_1 = t_{\min} + \frac{S}{G^* \sqrt{T^* + 1 + h_1} (1 - C_{\text{sat}})} \quad \text{and} \quad n \approx \hat{n}_2 = \frac{\exp\left\{-\lambda \left(\frac{1+h_1}{T^*} + 1\right)^{-3} \left[\ln\left(\frac{1}{C_{\text{sat}}}\right)\right]^{-2}\right\}}{\sqrt{T^* + 1 + h_1} (1 - C_{\text{sat}})},$$

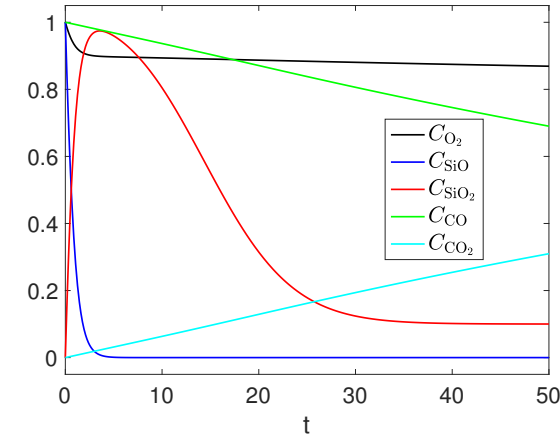
449 where  $\hat{n}_2$  is a constant and  $S = s^*(t) - s$  is the moving coordinate. Using parameter values from Table 2 as  
 450 well as  $C_{\text{sat}} = 0.1$ , we find  $\hat{n}_2 \approx 5.773 \times 10^{-1}$ , and scaling with  $J^*$  we have  $\hat{n}_2 \approx 5.773 \times 10^{-1} J^* = 8.879 \times 10^3$ ,  
 451 which is consistent with the value  $n$  levels off to in Figure 4c as  $S$  becomes  $\mathcal{O}(1)$  ( $n \approx \hat{n}_2$  corresponds to the  
 452 blue dashed line).

453 To summarise, the asymptotic solutions provide an explicit formula for  $n$  in terms of well-known parame-  
 454 ters, capturing the qualitative behaviour of the particle size distribution, with the small time ( $0 < t - t_{\min} \ll$   
 455  $1$ ) approximation  $\hat{n}_1(\hat{t}_1)$  capturing the peak and the intermediate time ( $1 \ll t - t_{\min} \ll \varepsilon^{-1}$ ) approximation  
 456  $\hat{n}_2(\hat{t}_1)$  providing the uniform distribution away from the peak. The largest timescale,  $t - t_{\min} \gg \varepsilon^{-1}$ , will  
 457 not play a strong role in modifying the distribution  $n$  (which is on the two timescales felt by  $C_{\text{SiO}_2}$ ), and  
 458 hence we do not consider it.

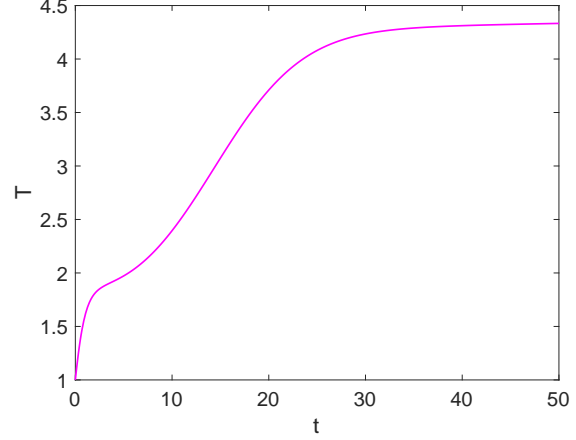
459 **3.3. Numerical solution of the fully-coupled system for  $\zeta_1, \zeta_2 > 0$ .** We solve the full problem  
 460 (19) with  $\zeta_1, \zeta_2 > 0$  numerically and then use the analytical solution obtained for  $n$  in Section 3.2, providing  
 461 simulations in Figure 5. The  $\text{SiO}_2$  concentration (red curve in Figure 5a) reaches a maximum while the  
 462  $\text{SiO}$  combustion reaction occurs, and later decreases as  $\text{SiO}_2$  is consumed due to particle growth. The  
 463 temperature, shown in Figure 5b, also increases initially due to the combustion reaction, yet further increases  
 464 due to energy given off during particle formation. The peak in the particle density function,  $n$ , plotted in  
 465 Figure 5d, moves to the right with time as particles grow. However, as the available  $C_{\text{SiO}_2}$  decreases toward  
 466 the saturation concentration (around  $t = 25$ ), the value of  $n = J/G$  at  $s = 1$  gets very large forming a second  
 467 peak around the smallest particle size. Many particles are created (due to the increasing temperature), but  
 468 they cannot grow large (due to the limited availability of  $\text{SiO}_2$ ). In Figure 5c we see that particle growth  
 469 stops after some critical time, and the maximum particle size is given by the value that the red characteristic  
 470 converges to, approximately 2.2 for the case plotted. In Figure 5e we plot the first few moments of the  
 471 distribution  $n$ , the number of particles,  $M_0$ , the mean,  $\mu = M_1/M_0$ , and the variance,  $\sigma^2 = M_2/M_0 - \mu^2$ .  
 472 All moments tend to a constant for  $t > 35$ , meaning that the particle density function converges to the red  
 473 curve in Figure 5f as  $C_{\text{SiO}_2} \rightarrow C_{\text{sat}} = 0.1$ . This curve corresponds to a bimodal distribution around the  
 474 minimum and maximum particle size.

475 The existence of such a bimodal distribution for particle size is in agreement with previous experimental  
 476 studies [11] where the particle size distribution of well dispersed microsilica was found to be bimodal, with  
 477 a submicron range of particle sizes containing most of the particle mass, and a micron range with fewer but  
 478 much larger particles. In order to illustrate this finding, in Figure 6 we show a SEM picture of a microsilica  
 479 sample where we can see few large particles with many small particles attached to them. As the value of  $C_{\text{sat}}$   
 480 increases the distribution turns almost uniform, since less particles are formed and their sizes are smaller  
 481 since the time interval on which the concentration of  $\text{SiO}_2$  is above saturation is reduced.

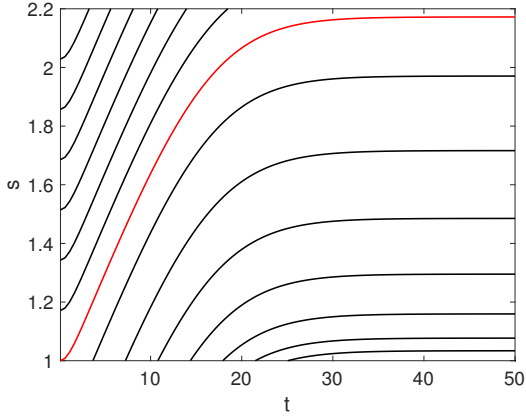
482 In Figure 7 we show both peaks on a semi-log plot. Notice that the order of the peaks in Figure 7  
 483 is the opposite to the one found in Figure 5d, and that the values on the horizontal axis of Figure 7b are  
 484 inverted. We use the same approximations as in Sections 3.2.1-3.2.2 to obtain an approximation for the large  
 485 particle-size peak (red dashed line) and uniform distribution between peaks (blue dashed line). However, in  
 486 the coupled case these approximations are only valid for early times, and the late time peak shown in 7b  
 487 (around  $s = 1$ ) is found numerically.



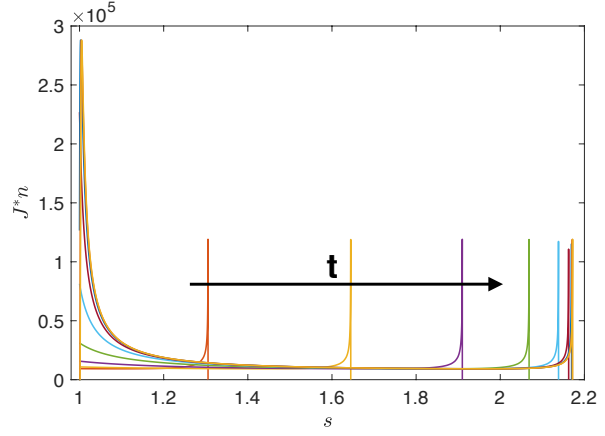
(a) Chemical concentrations



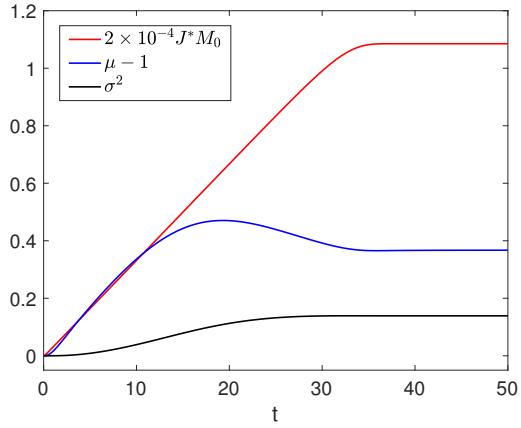
(b) Temperature



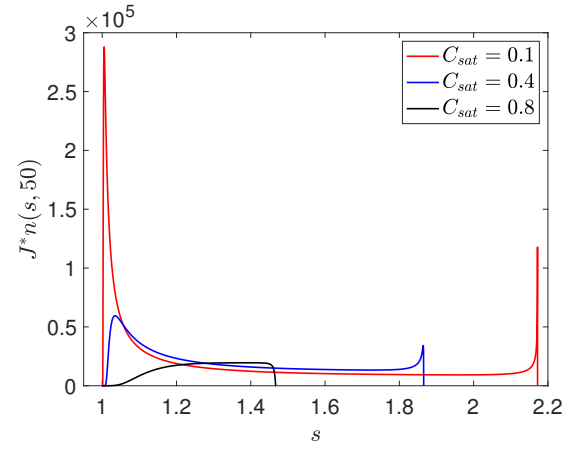
(c) Characteristic curves



(d) Number density functions



(e) Moments of the distributions for  $C_{\text{sat}} = 0.1$



(f) Final particle density function for different  $C_{\text{sat}}$

Fig. 5: Plot of the chemical concentrations (a), temperature (b), characteristic curves (c), number density functions (d), and properties of the density distribution (e) obtained from solving the fully-coupled ( $\zeta_1, \zeta_2 > 0$ ) problem (19) numerically, and using these results in (33) and (34). We take  $C_{\text{sat}} = 0.1$  and  $a = 0.2$ , with other parameters chosen from Table 2, and scale  $n$  with  $J^*$ . The direction of the arrow in (d) indicates increasing time from  $t_{\text{min}} = 0.106$  to  $t_{\text{min}} + 45$ , with an increment of 5 at every iteration. As  $C_{\text{sat}}$  is increased (f), particle formation initializes later, thus particles have less time to grow, and hence the distribution skews toward smaller sized particles at the final time  $t = 50$ . In (a) and (e), the legend indicates the meaning of each curve.

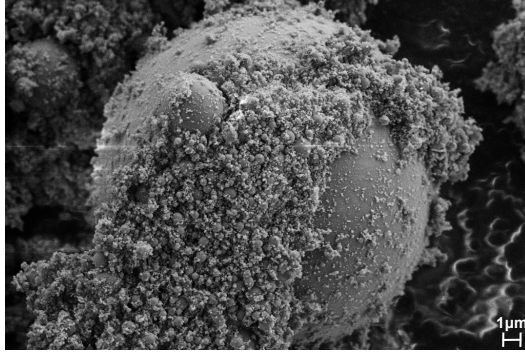


Fig. 6: SEM image of microsilia particles showing some large particles with many small particles attached to them. Image from Dr. Mari K. Næss [26].

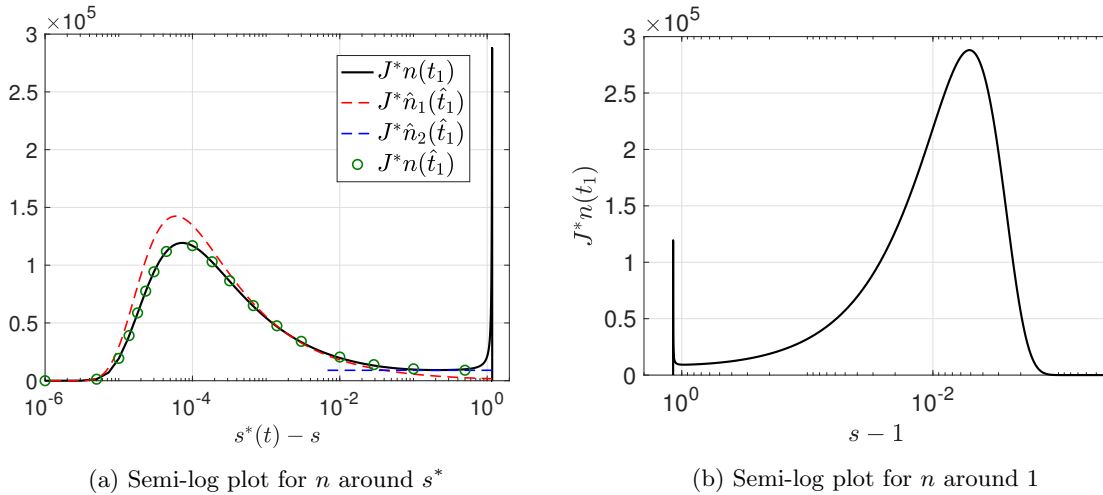


Fig. 7: Semi-log plots for the number density function around (a)  $s = s^*$  zooming in the large particle-size peak, and around (b)  $s = 1$  zooming in the small particle-size peak. In (a) we show the numerical results for  $n$  (black solid line), the real solution for  $n$  with asymptotic approximations for the characteristics as in the uncoupled case (green circles), and the asymptotic approximations for the peak (red dashed line) and uniform part (blue dashed line) taken from (41a) and (44) respectively, whereas in (b) we only show the numerical result. In (a) the legend indicates the meaning of each curve.

488 **4. The case of initially spatially separated chemical species.** In this section, we turn our at-  
489 tention to the configuration where chemical concentrations  $C_{O_2}$ ,  $C_{SiO}$ ,  $C_{CO}$  and temperature are initially  
490 spatially heterogeneous, with  $C_{O_2}$  present primarily in the region  $z > 0$ ,  $C_{SiO}$  and  $C_{CO}$  in the region  $z < 0$ ,  
491 with a small overlap. Hence, the dimensionless initial conditions for the concentrations and temperature are  
492 such that they are compatible with the following far-field behaviour

493 (45a) 
$$C_{O_2} = C_{SiO_2} = C_{CO_2} = 0, \quad C_{SiO} = C_{CO} = T = 1 \quad \text{as } z \rightarrow -\infty,$$

494 (45b) 
$$C_{O_2} = 1, \quad C_{SiO} = C_{CO} = T = 0, \quad \frac{\partial C_{SiO_2}}{\partial z} = \frac{\partial C_{CO_2}}{\partial z} = 0 \quad \text{as } z \rightarrow \infty,$$

495 This is analogous to adding large quantities of oxygen into the top or side of a furnace in more complicated  
496 geometries. For large enough temperatures to permit reactions, this configuration results in a narrow reaction  
497 layer which then evolves over time. The initial conditions for  $n$  and its moments remain unchanged.

498 **4.1. Analytical solution for the coupled chemical - temperature subsystem.** The set of equa-  
499 tions (14) constitute a nonlinear, nonlocal reaction-diffusion system. To make any progress outside of nu-

500 merical simulations, we shall need to make further simplifying assumptions. Firstly, we neglect the coupling  
501 to the moments, and set  $\zeta_1$  and  $\zeta_2$  to be equal to zero as in Section 3.1. We will include these coupling  
502 parameters later when obtaining numerical simulations and compare them to the asymptotic solutions. Fur-  
503 ther, since  $\varepsilon < \zeta_1$  by an order of magnitude, we set  $\varepsilon = 0$  and neglect the slower reaction. Finally, observing  
504 that  $d_{\text{SiO}, \text{Le}} = \mathcal{O}(1)$ , we set  $d_{\text{SiO}} = \text{Le} = 1$  in order to have equal diffusion rates, which greatly simplifies  
505 the derivations. Under these assumptions, the equations governing the dominant reaction are

$$506 \quad (46a) \quad \frac{\partial C_{\text{O}_2}}{\partial t} - \frac{\partial^2 C_{\text{O}_2}}{\partial z^2} = -\frac{a}{2} f_1(T) C_{\text{O}_2} C_{\text{SiO}},$$

$$507 \quad (46b) \quad \frac{\partial C_{\text{SiO}}}{\partial t} - \frac{\partial^2 C_{\text{SiO}}}{\partial z^2} = -f_1(T) C_{\text{O}_2} C_{\text{SiO}},$$

$$508 \quad (46c) \quad \frac{\partial T}{\partial t} - \frac{\partial^2 T}{\partial z^2} = h_1 f_1(T) C_{\text{O}_2} C_{\text{SiO}}.$$

510 Defining the quantities  $w_1(z, t) = C_{\text{O}_2} - \frac{a}{2} C_{\text{SiO}}$  and  $w_2(z, t) = T + h_1 C_{\text{SiO}}$ , we find from (45)-(46) that

$$511 \quad (47a) \quad \frac{\partial w_1}{\partial t} - \frac{\partial^2 w_1}{\partial z^2} = 0, \quad w_1 \rightarrow 1 \quad \text{as } z \rightarrow \infty, \quad w_1 \rightarrow -\frac{a}{2} \quad \text{as } z \rightarrow -\infty,$$

$$512 \quad (47b) \quad \frac{\partial w_2}{\partial t} - \frac{\partial^2 w_2}{\partial z^2} = 0, \quad w_2 \rightarrow 0 \quad \text{as } z \rightarrow \infty, \quad w_2 \rightarrow 1 + h_1 \quad \text{as } z \rightarrow -\infty.$$

514 Solving (47) with appropriate Heaviside functions centred at  $z = 0$  as initial data, we find

$$515 \quad (48a) \quad w_1(z, t) = \frac{1 + \text{erf}(\eta)}{2} - \frac{a(1 - \text{erf}(\eta))}{4} = \phi(\eta) - \frac{a}{2} \phi(-\eta),$$

$$516 \quad (48b) \quad w_2(z, t) = (1 + h_1) \frac{1 - \text{erf}(\eta)}{2} = (1 + h_1) \phi(-\eta),$$

518 where  $\eta = \frac{z}{2\sqrt{t}}$  is the similarity variable and  $\phi(\eta) = \frac{1}{2}(1 + \text{erf}(\eta))$ . From the definitions of  $w_1$  and  $w_2$ , we  
519 determine that

$$520 \quad (49) \quad C_{\text{O}_2} = \phi(\eta) - \frac{a}{2} (\phi(-\eta) - C_{\text{SiO}}) \quad \text{and} \quad T = \phi(-\eta) + h_1 (\phi(-\eta) - C_{\text{SiO}}).$$

521 We now search for a solution of the form  $C_{\text{SiO}}(z, t) = u(\eta, \tau)$ ,  $\eta = \frac{z}{2\sqrt{t}}$ ,  $\tau = t$ , and using (49), this puts  
522 (46b) into the form

$$523 \quad (50) \quad \frac{\partial u}{\partial \tau} - \frac{1}{4\tau} \left( \frac{\partial^2 u}{\partial \eta^2} + 2\eta \frac{\partial u}{\partial \eta} \right) = -f_1 (\phi(-\eta) + h_1 (\phi(-\eta) - u)) \left( \phi(\eta) - \frac{a}{2} (\phi(-\eta) - u) \right) u.$$

524 In the small-time limit  $\tau \rightarrow 0^+$ , a solution is only possible if

$$525 \quad (51) \quad \frac{\partial^2 u}{\partial \eta^2} + 2\eta \frac{\partial u}{\partial \eta} = 0 \quad \text{as } \tau \rightarrow 0^+,$$

526 and using the conditions (45), we find that  $u \sim \Phi(-\eta)$  as  $\tau \rightarrow 0^+$ , that is,  $C_{\text{SiO}}(z, t) \sim \phi(-\frac{z}{2\sqrt{t}})$ ,  $C_{\text{O}_2} \sim$   
527  $\phi(\frac{z}{2\sqrt{t}})$ , and  $T \sim \phi(-\frac{z}{2\sqrt{t}})$  as  $t \rightarrow 0^+$ . Thus the heat and mass transfer mechanism is diffusion away from  
528 tial conditions.

529 In the long time limit  $\tau \rightarrow \infty$ , we must resolve a moving front which corresponds to the reaction  
530 zone. Motivated in part by the application of similar approaches to other reaction-diffusion systems in the  
531 literature [5, 8, 9, 16], we consider a WKB approximation in order to resolve the sharp front, taking the  
532 ansatz  $u(\eta, \tau) = \exp(-v(\eta, \tau))$ , with  $v(\eta, \tau) = \mathcal{O}(\tau^\beta)$  for some  $\beta > 0$  to be determined. As the phase term  
533  $v$  grows, localized rapid decay of the exponential results in a moving front. Using the WKB ansatz in (50),  
534 and neglecting the small parameter  $a$  (as we did in Section 3.1.3), equation (50) becomes

$$535 \quad (52) \quad \frac{\partial v}{\partial \tau} + \frac{1}{4\tau} \left( \left( \frac{\partial v}{\partial \eta} \right)^2 - \frac{\partial^2 v}{\partial \eta^2} - 2\eta \frac{\partial v}{\partial \eta} \right) = f_1 ((1 + h_1) \phi(-\eta)) \phi(\eta) + \mathcal{R},$$

536 where the error term  $\mathcal{R} = [f_1((1+h_1)\phi(-\eta) - h_1u) - f_1((1+h_1)\phi(-\eta))\phi(\eta)]\phi(\eta)$  results from omitting  
 537 the explicit dependence of  $u$  in the argument of  $f_1$  term given in (50). We expand  $v$  as

$$538 \quad (53) \quad v(\eta, \tau) = \tau^\beta \sum_{\ell=0}^{\infty} \tau^{-\beta\ell} V_\ell(\eta) \quad \text{as } \tau \rightarrow \infty,$$

539 and placing this into (52), we obtain the dominant balances which determine  $\beta$ : The time derivative term is  
 540  $\mathcal{O}(\tau^{\beta-1})$ , the dominant diffusion term is  $\mathcal{O}(\tau^{2\beta-1})$ , and the reaction term is  $\mathcal{O}(\tau^0)$ . Of the three possibilities,  
 541 only the balance between the dominant diffusion term and the reaction kinetics is consistent with our  
 542 assumptions and gives a value of  $\beta > 0$ . Taking the resulting  $\beta = 1/2$  and placing (53) into (52), we find

$$543 \quad (54) \quad \frac{1}{4} \left( \frac{dV_0}{d\eta} \right)^2 + \frac{\tau^{-1/2}}{2} \left( V_0 - \eta \frac{dV_0}{d\eta} - \frac{1}{2} \frac{d^2V_0}{d\eta^2} + \frac{dV_0}{d\eta} \frac{dV_1}{d\eta} \right) + \mathcal{O}(\tau^{-1}) = f_1((1+h_1)\phi(-\eta))\phi(\eta) + \mathcal{R}.$$

544 Within the reaction zone,  $u = \mathcal{O}(e^{-\sqrt{\tau}})$  and  $\eta = \mathcal{O}(1)$ . Since  $f_1$  in (15) is positive and bounded with  
 545 bounded derivative, there exists  $\mathcal{O}(1)$  constant  $R_0 > 0$  such that  $|\mathcal{R}| < R_0\phi(\eta)u = \mathcal{O}(e^{-\sqrt{\tau}})$ , and hence  $\mathcal{R}$  is  
 546 exponentially small within the reaction zone. To the left of the reaction zone,  $u = \mathcal{O}(1)$  and  $\eta \gg 1$ . In this  
 547 region,  $\phi(\eta) < e^{-\eta^2}$  while  $0 \leq u \leq \phi(-\eta) \leq 1$ , so  $|\mathcal{R}| < [f_1(1+h_1) - f_1(0)]e^{-\eta^2} = \mathcal{O}(e^{-\eta^2})$ , and hence  $\mathcal{R}$  is  
 548 exponentially small in this region, as well. As the expansion (53) is algebraic, the exponentially small term  
 549  $\mathcal{R}$  is subdominant at each order in the expansion (53), and can be ignored when solving (54).

550 At leading order,  $\mathcal{O}(1)$ , we see that (54) gives

$$551 \quad (55) \quad \frac{1}{4} \left( \frac{dV_0}{d\eta} \right)^2 = f_1((1+h_1)\phi(-\eta))\phi(\eta).$$

552 Solving for  $V_0$  and taking the positive root (so that the expansion in the WKB ansatz gives decay rather  
 553 than blow-up at large time), we find

$$554 \quad (56) \quad V_0(\eta) = 2 \int_{-\infty}^{\eta-\eta_0} \sqrt{f_1((1+h_1)\phi(-\sigma))\phi(\sigma)} d\sigma.$$

555 Since information about the initial configuration is lost in this long time limit, we have taken  $\eta - \eta_0$  as the  
 556 upper limit of the integral (56). Exploiting such shift in the similarity variable can prove useful, and for our  
 557 purposes we will use it to calibrate the large-time asymptotics to numerical simulations of the exact solution.

558 We then have  $u(\eta, \tau) = \exp(-\tau^{1/2}V_0(\eta) + \mathcal{O}(1))$  as  $\tau \rightarrow \infty$ . For large yet finite  $\tau$ ,  $\lim_{\eta \rightarrow -\infty} u = 1$  while  
 559  $\lim_{\eta \rightarrow \infty} u = 0$ , in agreement with the boundary conditions on  $C_{\text{SiO}}$ , so no additional scaling of  $u$  is required  
 560 at leading order. The next order correction,  $V_1(\eta)$ , will slightly correct the core structure near the moving  
 561 front, but we find agreement with numerics is already good at leading order, and omit higher order terms  
 562 for sake of brevity. Having determined the large-time asymptotics for  $C_{\text{SiO}}$ , we construct an approximate  
 563 solution for (46),

$$564 \quad (57) \quad \begin{aligned} C_{\text{SiO}}(z, t) &\sim \exp\left(-\sqrt{t}V_0\left(\frac{z}{2\sqrt{t}}\right)\right), & C_{\text{O}_2}(z, t) &\sim \phi\left(\frac{z}{2\sqrt{t}}\right), & \text{and} \\ T(z, t) &\sim \phi\left(-\frac{z}{2\sqrt{t}}\right)(1+h_1) - h_1 \exp\left(-\sqrt{t}V_0\left(\frac{z}{2\sqrt{t}}\right)\right) & \text{as } t &\rightarrow \infty. \end{aligned}$$

565 The latter two quantities follow from (49), and the fact that the temperature both depends on diffusion and  
 566 also a source which involves the asymptotic solution for  $C_{\text{SiO}}$ . We solve the initial-boundary value problem  
 567 (46) numerically by the method of lines, discretising the PDEs in space and integrating the resulting ODEs  
 568 in time. We use appropriate Heaviside functions centred at the origin as initial data in the numerics. As  
 569 there will in general be an offset in the large-time asymptotics as large time expansions neglect initial data,  
 570 we calibrate the asymptotics to the simulations by choosing  $\eta_0$  to match both the asymptotic solution and  
 571 the numerics at the unique value of  $z$  where  $C_{\text{SiO}} = 0.5$  for  $t = 100$ , finding  $\eta_0 = 0.32$ . In Figure 8 we  
 572 compare both the asymptotic solution (solid lines) and the numerical result (dashed lines), showing that the  
 573 agreement between the two solutions remains good as time increases.

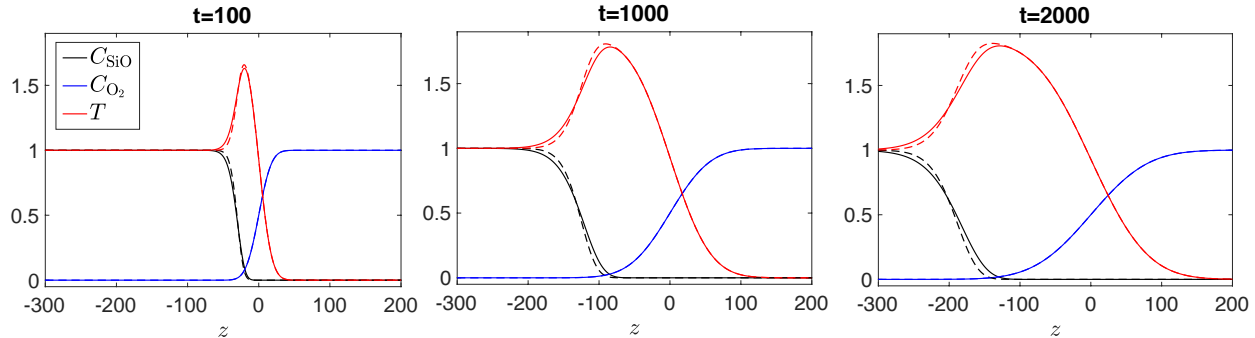


Fig. 8: Plot of the approximate asymptotic solution (57) (solid lines) and numerical simulation (dashed lines) for SiO (black) and O<sub>2</sub> (blue) concentrations, and temperature (red), as indicated in the legend, from solving problem (46).

574 We observe the reaction front moving to the left as SiO is being consumed by the combustion reaction  
 575 with the much more plentiful ( $a \ll 1$ ) oxygen. Due to its relative abundance, the oxygen slowly spreads due  
 576 to diffusion, with a relatively small proportion of the oxygen reacting with SiO. The temperature behind  
 577 the reaction front grows rapidly over time due to the combustion reaction, before levelling off to  $T \sim 1 + h_1$   
 578 within the core region as the reaction slows. The hot reaction zone broadens as the front moves toward the  
 579 left, with much of the new reactions between SiO and oxygen occurring near the front.

580 **4.2. Analytical solution of the particle density equation.** As the parameter  $d_p \approx 10^{-6}$ , molecular  
 581 diffusion is negligible relative to the chemical and thermal diffusivities in equation (18a), thus the resulting  
 582 PDE is equivalent to (21a). Therefore, the analytical solution is similar to the one found for the case of  
 583 initially well-mixed chemical species, but with an additional  $z$  dependence arising from the spatial variations  
 584 in  $C_{\text{SiO}_2}$  and  $T$ . Let  $C_{\text{SiO}_2}(z, t_{\min}(z)) = C_{\text{sat}}$ , then the solution is given by

$$585 \quad (58) \quad n = \frac{J(z, t_1)}{G(z, t_1)} \quad \text{with} \quad s = 1 + G^* \int_{t_1}^t G(z, \tau) d\tau, \quad t_1 > t_{\min}(z),$$

586 for  $t > t_{\min}(z)$ . The solution is  $n = 0$  for  $t \leq t_{\min}(z)$ . Notice that in this case we need to be careful with the  
 587 domain of definition of the solution since the value of  $t_{\min}$  depends on  $z$ .

588 **4.3. Numerical solution of the fully coupled model for  $\zeta_1, \zeta_2 > 0$ .** Similar to what was done in  
 589 Section 3.3 in the well-mixed case, we solve the system (14) for initially separated initial data numerically  
 590 and then use these results in the analytical solution for  $n$  found in Section 4.2. We follow the same numerical  
 591 scheme outlined at the end of Section 4.1, that is, the method of lines. This method involves discretising all  
 592 PDEs in (14) in space while leaving the time variable continuous, which leads to a larger system of ordinary  
 593 differential equations that is then numerically integrated in time. We plot numerical solutions for  $C_{\text{SiO}_2}$  and  
 594  $T$  in Figure 9 for both  $\zeta_1 = \zeta_2 = 0$  (left) and  $\zeta_1, \zeta_2 > 0$  (right), comparing each side-by-side at different values  
 595 of time. In both cases there is initially zero concentration of SiO<sub>2</sub>, and after a critical time the concentration  
 596 increases and starts spreading slightly toward the left since it forms from the reaction between O<sub>2</sub> and SiO,  
 597 moving left with the reaction region as shown in Figure 8. In the case of  $\zeta_1, \zeta_2 > 0$ , where we include  
 598 a sink of SiO<sub>2</sub> due to the particle formation (Figure 9b), the concentration of SiO<sub>2</sub> decreases after time,  
 599 since  $C_{\text{SiO}_2}$  is used up and rate limiting. In both cases the temperature increases with time, however, when  
 600  $\zeta_1, \zeta_2 > 0$ , heat is released during the particle formation process, and the extent of the temperature increase  
 601 within the reaction zone is much greater. Therefore, although the asymptotic solutions are reasonable for  
 602 a qualitative understanding of the dynamics, including the coupling of the particle growth back into the  
 603 chemical-temperature system ( $\zeta_1, \zeta_2 > 0$ ) is needed for quantitative accuracy, and to determine how fast  
 604 SiO<sub>2</sub> is used in particle formation and growth. One can therefore view the  $\zeta_1 = \zeta_2 = 0$  limit as modelling a  
 605 situation where there is plentiful SiO<sub>2</sub> which is never used up due to a slow rate of particle growth, whereas  
 606 the case of  $\zeta_1, \zeta_2 > 0$  models the situation where SiO<sub>2</sub> is strongly rate limited, and is used up in particle  
 607 growth more rapidly than it is produced in the reaction zone.

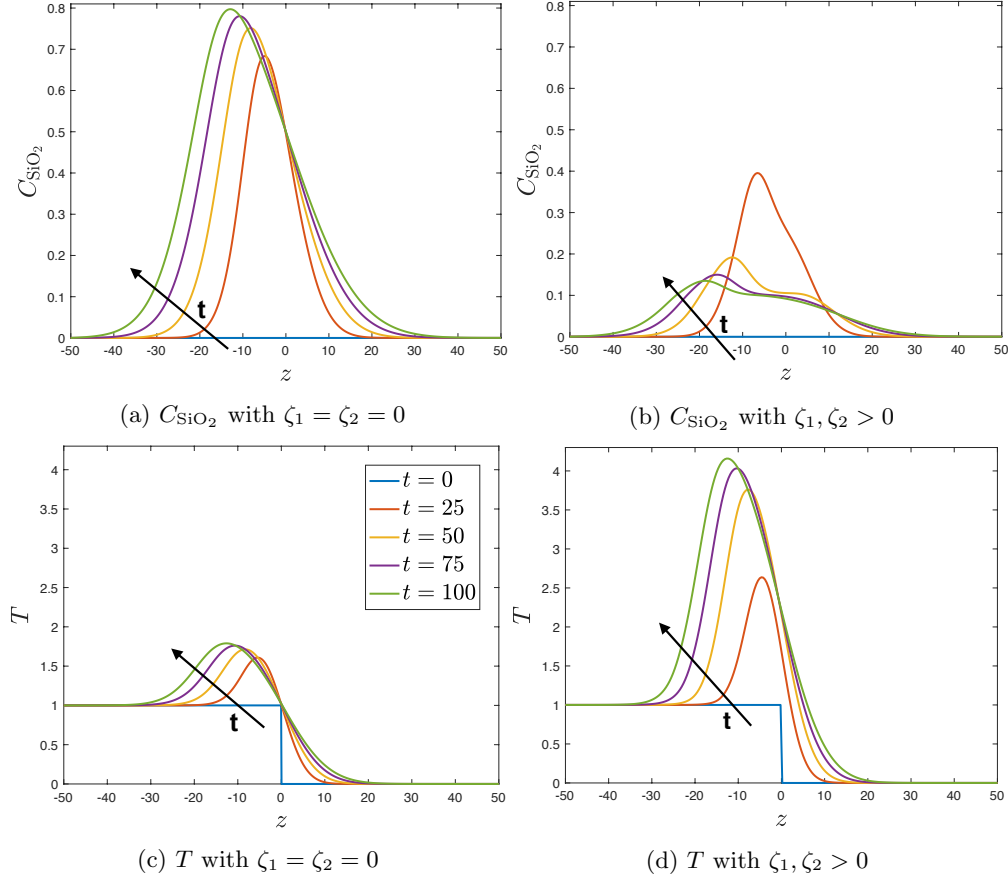


Fig. 9: (a,b) Concentration of  $\text{SiO}_2$  ( $C_{\text{SiO}_2}$ ) and (c,d) temperature variations in  $z$ , for different times equally spaced from  $t = 0$  to 100 as shown in the legend in (c). This is for the case  $\zeta_1 = \zeta_2 = 0$  in (a,c), and  $\zeta_1, \zeta_2 > 0$  in (b,d). We choose  $a = 0.2$ ,  $C_{\text{sat}} = 0.1$ , with all other parameters as given in Table 2.

608 To better understand properties of the particle distribution,  $n$ , we use the numerical solution for the  
 609 chemistry-temperature system in the analytical formula (58) for  $n$ , and plot  $J^*n$  over  $s$  and  $z$  for various  
 610 time values in Figure 10. The largest particles (largest  $s$ ) are located in the center of the reaction zone (as  
 611 they have had time to grow), whereas smaller, newly formed particles are located near the boundary of the  
 612 zone. The region with particles ( $n > 0$ ) grows in spatial extent with the reaction zone, and the highest  
 613 density of particles is at the boundary near the reaction front. In the case where there is coupling of the  
 614 particle growth back into the chemistry-temperature system,  $\zeta_1, \zeta_2 > 0$ , we observe a resurgence of small  
 615 particles being formed over the entire reaction zone, rather than just near the boundary (see lower right  
 616 panel of Figure 10). We hypothesise that this originates from the comparatively high temperatures arising  
 617 in the fully coupled system, which results in the last of the  $\text{SiO}_2$  being used up to rapidly make smaller  
 618 particles, after which point the process ends as  $\text{SiO}_2$  is depleted, with these particles growing no further.  
 619 Our theoretical results showing a build-up of smaller particles (in addition to the existing larger particles)  
 620 are in agreement with earlier experimental findings [27].

621 The mean and variance of the particle distribution are shown in Figure 11. The mean size of the particles,  
 622 as well as their variance, is larger when  $\zeta_1, \zeta_2 = 0$ , since in this case there is more  $\text{SiO}_2$  produced than is  
 623 used in particle formation. This is also apparent from Figure 10. In contrast, when  $\zeta_1, \zeta_2 > 0$ , the  $\text{SiO}_2$   
 624 is used in finite time, hence there is less material available for particle growth, and smaller particles result.  
 625 Panels on the right-hand side of Figure 11 are akin to spatial generalizations of the well-mixed case shown  
 626 in Figure 5e.

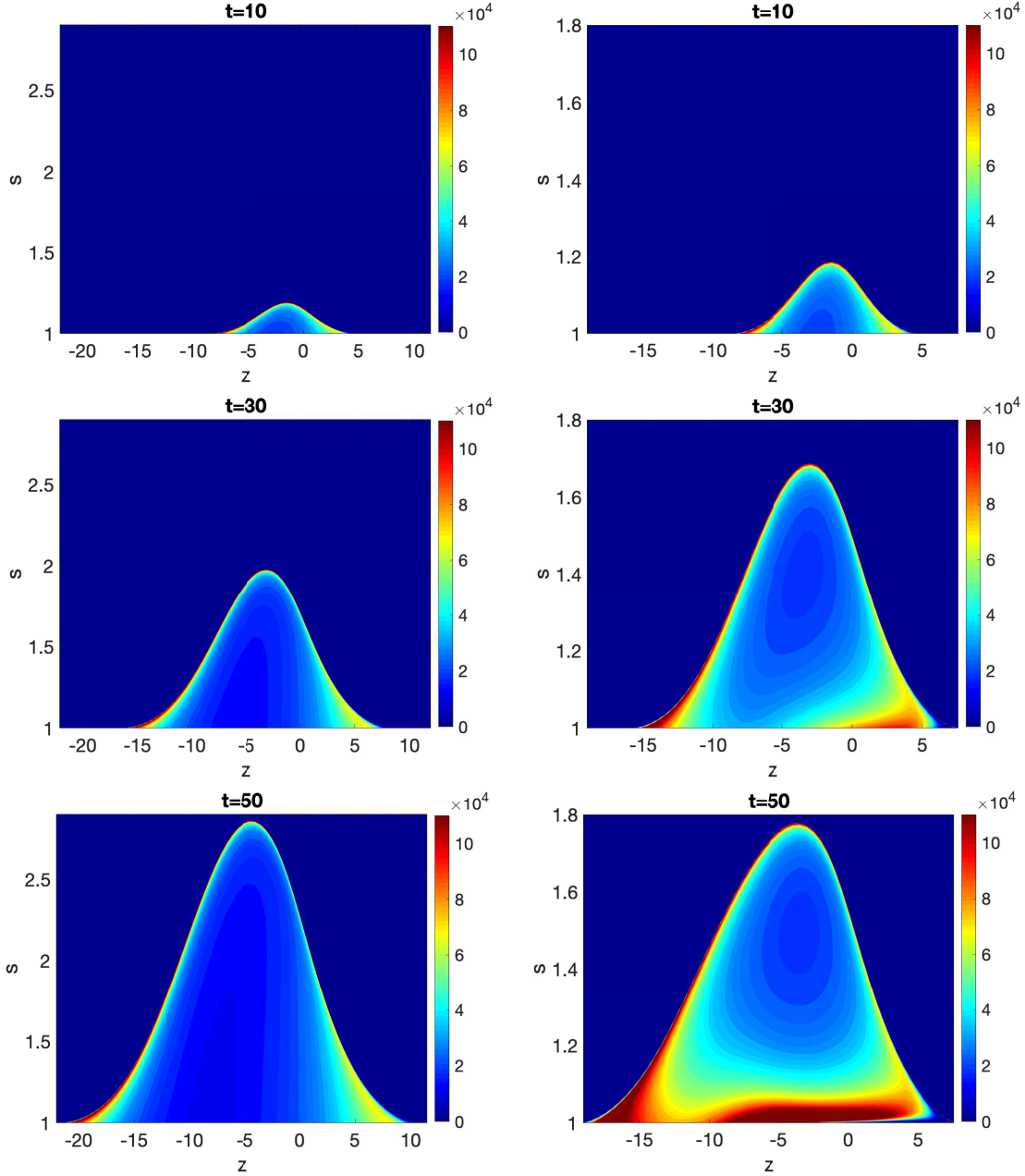


Fig. 10: Heat maps for  $J^*n$  with respect to  $s$  and  $z$ , for different values of time. This is for the case  $\zeta_1 = \zeta_2 = 0$  (left) and  $\zeta_1, \zeta_2 > 0$  (right). We choose  $a = 0.2$ ,  $C_{\text{sat}} = 0.1$ , with all other parameters as given in Table 2.

627 **5. Discussion.** Motivated by microsilica particle formation inside a silicon furnace hood, we derived a  
 628 mathematical model consisting of a heat and mass transfer system associated with two dominant chemical  
 629 reactions taking place within the furnace coupled to a population balance equation for microsilica particle  
 630 formation and growth. The material consumed and heat released due to particle formation was also coupled  
 631 back to the relevant mass and energy conservation equations. After simplifying the geometry, we studied a  
 632 one-dimensional model in space for the dynamics near, within, and around the reaction zone or flame. Making  
 633 a variety of simplifying assumptions and considering various cases for the coupling of particle growth with  
 634 the heat and mass transfer system, we arrived at an assortment of asymptotic and numerical results which

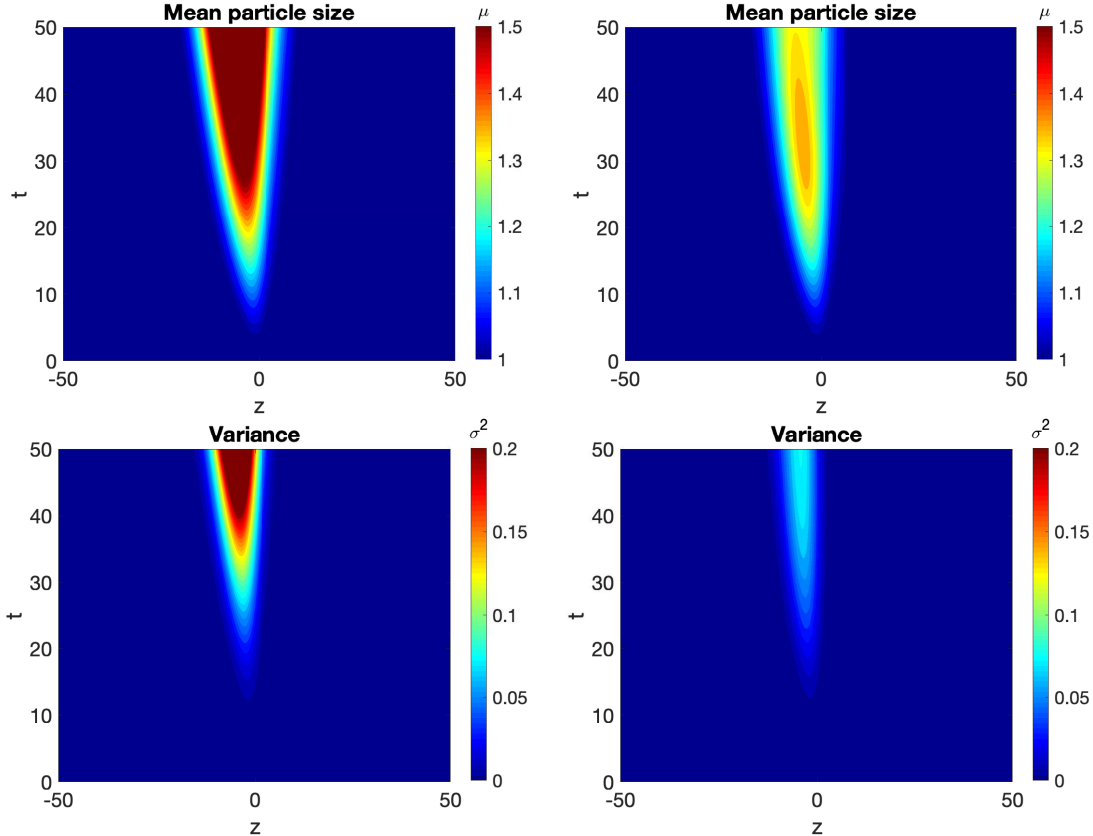


Fig. 11: Heat maps for  $\mu$  and  $\sigma^2$  from top to bottom with respect to  $t$  and  $z$ . The figures on the left are for the case  $\zeta_1 = \zeta_2 = 0$ , and the ones on the right for  $\zeta_1, \zeta_2 > 0$ . We choose  $a = 0.2$ ,  $C_{\text{sat}} = 0.1$ , with all other parameters as given in Table 2.

635 give insight into the physical processes resulting in microsilica formation.

636 We first considered a configuration where the chemical species are well-mixed, and hence diffusion plays  
637 no role, with this case modelling dynamics most valid on a small lengthscale within the reaction zone.  
638 In the case where the mass and energy equations are coupled into the particle growth equation, but not  
639 the other way around ( $\zeta_1 = \zeta_2 = 0$ ), we obtained asymptotic solutions for small  $a$ , that is for an oxygen  
640 rich environment (which is the physically relevant limit), and these compared favourably with numerical  
641 simulations. The SiO reaction occurs much faster than the CO reaction, and if enough oxygen is available,  
642 all of the initial SiO will be consumed hence the same number of moles of SiO<sub>2</sub> will be produced. As the  
643 sink term in the mass conservation was neglected, particles continued to grow since the particle mass was  
644 negligible to the total mass of SiO<sub>2</sub> remaining. However, when the particle growth process was coupled back  
645 to the mass and energy conservation ( $\zeta_1, \zeta_2 > 0$  in which case only numerical simulations were possible),  
646 we observed that the number and size of particles formed was limited, with particle growth ending once the  
647 mass of SiO<sub>2</sub> was depleted. Therefore, the asymptotics obtained for  $\zeta_1 = \zeta_2 = 0$  and  $a \ll 1$  are most useful  
648 either for understanding early-time dynamics (before SiO<sub>2</sub> is depleted due to particle formation and growth),  
649 or in the regime where O<sub>2</sub> is plentiful, and the rate of depletion of SiO<sub>2</sub> is small (*i.e.*, when the reaction  $R_1$   
650 in (1) produces a sufficiently large quantity of SiO<sub>2</sub> so that it is not depleted rapidly by the sink term (10)).  
651 The sink term (10) therefore sets the timescale for the fully coupled system. An additional finding was that  
652 our solutions result in a bimodal size distribution of microsilica particles, with a submicron range of particle  
653 sizes containing most of the particle mass, and a micron range with fewer but much larger particles, and this  
654 finding is consistent with experimental results present in the literature [11].

655 In the second configuration that we studied, the chemical species are initially spatially separated, with  
656 O<sub>2</sub> plentiful on one side of the domain, and the other chemical species plentiful on the other side of the

657 domain. Given an initial temperature distribution characteristic of what is found in a cross-section of a  
 658 furnace, reactions occur within a narrow reaction zone. As  $O_2$  is the most plentiful of the fuel components,  
 659 the reaction zone will propagate toward the other fuel components through diffusion. We observe that the  
 660 dynamics within the core of the reaction zone are indeed similar to those of the spatially well-mixed case,  
 661 verifying our intuition that the well-mixed case is indeed a simple yet effective representation of the dynamics  
 662 within the flame. The longest-lived and largest particles arise in the center of the reaction zone, where  $SiO_2$   
 663 is most abundant, and these match best with the predictions from the well-mixed limit. Meanwhile, the full  
 664 spatial model is useful for better understanding the distribution of particles sizes over space and time, with  
 665 gradually smaller particles being produced toward the boundary of the reaction zone.

666 We conclude that  $O_2$  availability and a sufficiently high temperature are essential for the combustion  
 667 reactions to occur, strongly influencing both the width of the reaction zone and the particle size distribution.  
 668 A decrease in the availability of  $O_2$  results in a more narrow reaction zone, and hence limits  $SiO_2$  production  
 669 over a given time interval. Regarding industrial scale processes which motivate our work, this finding suggests  
 670 operators to provide adequate inflow of  $O_2$ , particularly if larger  $SiO_2$  particles are sought. In addition, we  
 671 find that increasing the saturation or equilibrium concentration of  $SiO_2$  (for instance, by decreasing  $T$ ) will  
 672 result in a decrease in mean particle size, although this parameter depends on other environmental factors,  
 673 and may be more challenging to control in practical applications.

674 Our work provides a qualitative underlying of the physical processes at play when microsilica is produced,  
 675 yet in order to improve the quantitative agreement with experiments and real-world furnace observations,  
 676 there are some extensions to consider in future work. The most immediate extension is to couple the model  
 677 we have developed to a momentum equation for the flow of gas within the furnace. While we have considered  
 678 the velocity to be uniform, and hence scaled it out of the problem, the fluid problem is in practice more  
 679 dynamic, with preliminary simulations suggesting the emergence of eddies and related localized structures,  
 680 which may trap particles, allowing them to recirculate through reaction zones multiple times before they  
 681 are ejected from the furnace through the exhaust pipe. In related applications, microscopic zones where  
 682 individual particles grow may be several orders of magnitude smaller than macroscopic turbulent eddies [41],  
 683 with the reaction zones highly localized within the turbulent flow. This suggests that the narrow reaction  
 684 zones we study will likely still exist within the larger flow, embedded within boundary layers formed near  
 685 the interface of  $O_2$  and  $SiO$ . There is recent work modelling fine-particle formation in turbulent flames [30],  
 686 large-scale simulation of aerosol nucleation and growth in turbulent mixing layers [45], and Favre-averaged  
 687 population balance equations for turbulent flames [46], and some of these approaches may prove useful. More  
 688 complex and realistic geometries for the furnace should also be considered, since the geometry of the problem  
 689 domain will influence the flow problem, even if domain geometry does not strongly modify dynamics within  
 690 the reaction zone, which is orders of magnitude smaller.

691

## REFERENCES

- 692 [1] D. ALEXANDROV, *Nucleation and crystal growth in binary systems*, Journal of Physics A: Mathematical and Theoretical,  
 693 47 (2014), p. 125102.
- 694 [2] A. ANIKIN, G. GALEVSKY, V. RUDNEVA, E. NOZDRIN, AND S. GALEVSKY, *Development of scientific and technological*  
 695 *bases for application of brown coal semi coke in the technology of non-milled silicon carbide*, in IOP Conference  
 696 Series: Materials Science and Engineering, vol. 150, IOP Publishing, 2016, p. 012005.
- 697 [3] C. ARTELT, H.-J. SCHMID, AND W. PEUKERT, *Modelling titania formation at typical industrial process conditions: effect*  
 698 *of surface shielding and surface energy on relevant growth mechanisms*, Chemical Engineering Science, 61 (2006),  
 699 pp. 18–32.
- 700 [4] A. BERMÚDEZ, J. L. FERRÍN, AND S. A. HALVORSEN, *Process models for the production of microalumina*, tech. report, 97  
 701 European Study Group with Industry, Santiago de Compostela, 2013.
- 702 [5] E. BOUIN, V. CALVEZ, N. MEUNIER, S. MIRRAHIMI, B. PERTHAME, G. RAOUL, AND R. VOITURIEZ, *Invasion fronts with*  
 703 *variable motility: phenotype selection, spatial sorting and wave acceleration*, Comptes Rendus Mathématique, 350  
 704 (2012), pp. 761–766.
- 705 [6] F. BROSA PLANELLA, C. P. PLEASE, AND R. A. VAN GORDER, *Extended stefan problem for solidification of binary alloys*  
 706 *in a finite planar domain*, SIAM Journal on Applied Mathematics, 79 (2019), pp. 876–913.
- 707 [7] J. BUCKMASTER, *The Mathematics of Combustion*, Frontiers in Applied Mathematics, Society for Industrial and Applied  
 708 Mathematics, 1985.
- 709 [8] D. S. COHEN, F. C. HOPPENSTEADT, AND R. M. MIURA, *Slowly modulated oscillations in nonlinear diffusion processes*,  
 710 SIAM Journal on Applied Mathematics, 33 (1977), pp. 217–229.
- 711 [9] C. CUESTA AND J. KING, *Front propagation in a heterogeneous Fisher equation: the homogeneous case is non-generic*,  
 712 The Quarterly Journal of Mechanics & Applied Mathematics, 63 (2010), pp. 521–571.

- 713 [10] E. DINGSØYR, M. DÅSTØL, AND W. WEDBERG, *Particle size and particle size distribution of elkem microsilica and*  
714 *its relevance to technical application*, in Proceedings of the 5th European Symposium Particle Characterization,  
715 Nurnberg, Germany, 1992, pp. 24–26.
- 716 [11] E. DINGSØYR, M. DÅSTØL, AND W. C. WEDBERG, *Particle size and particle size distribution of elkem microsilica and its*  
717 *relevance to technical application*, in European Symposium particle characterization, Germany, 1992.
- 718 [12] ELKEM. Personal communication.
- 719 [13] R. C. FLAGAN AND M. M. LUNDEN, *Particle structure control in nanoparticle synthesis from the vapor phase*, Materials  
720 Science and Engineering: A, 204 (1995), pp. 113–124.
- 721 [14] R. C. FLAGAN AND J. H. SEINFELD, *Fundamentals of air pollution engineering*, Courier Corporation, 2012.
- 722 [15] S. HALVORSEN, *A unidimensional dynamic model for the(ferro) silicon process*, in Electric Furnace Conference Proceed-  
723 ings., vol. 50, 1992, pp. 45–59.
- 724 [16] L. N. HOWARD AND N. KOPELL, *Slowly varying waves and shock structures in reaction-diffusion equations*, Studies in  
725 Applied Mathematics, 56 (1977), pp. 95–145.
- 726 [17] M. KADKHODABEIGI, H. TVEIT, AND K. BERGET, *Silicon process-new hood design for tapping gas collection*, in Twelfth  
727 International Ferroalloys Congress, 2010, pp. 109–119.
- 728 [18] N. E. KAMFJORD, *Mass and Energy Balances of the Silicon Process - Improved Emission Standards*, PhD thesis, Norwegian  
729 University of Science and Technology, 2012.
- 730 [19] D. KRAUSE AND H. LOCH, *Mathematical simulation in glass technology*, Springer Science & Business Media, 2012.
- 731 [20] B. LEE, J. JEONG, J. HWANG, M. CHOI, AND S. CHUNG, *Analysis of growth of non-spherical silica particles in a counterflow*  
732 *diffusion flame considering chemical reactions, coagulation and coalescence*, Journal of aerosol science, 32 (2001),  
733 pp. 165–185.
- 734 [21] H. LIM, T. KIM, S. EOM, Y.-I. SUNG, M. MOON, AND D. LEE, *Vaporization process of SiO<sub>2</sub> particles for slurry injection*  
735 *in inductively coupled plasma atomic emission spectrometry*, Journal of Analytical Atomic Spectrometry, 17 (2002),  
736 pp. 109–114.
- 737 [22] J. LOTHE AND G. M. POUND, *Reconsiderations of nucleation theory*, The Journal of Chemical Physics, 36 (1962), pp. 2080–  
738 2085.
- 739 [23] B. LUND, B. FOSS, K. LØVÅSEN, AND B. YDSTIE, *Sensitivity analysis of a dynamic model for submerged arc silicon*  
740 *furnaces*, in Proceedings: Tenth International Ferroalloys Congress, vol. 1, 2004, p. 4.
- 741 [24] E. V. MAKOVEEVA AND D. V. ALEXANDROV, *A complete analytical solution of the Fokker-Planck and balance equations*  
742 *for nucleation and growth of crystals*, Philosophical Transactions of the Royal Society A, 376 (2018), p. 20170327.
- 743 [25] W. MASSMAN, *A review of the molecular diffusivities of H<sub>2</sub>O, CO<sub>2</sub>, CH<sub>4</sub>, CO, O<sub>3</sub>, SO<sub>2</sub>, NH<sub>3</sub>, N<sub>2</sub>O, NO, and NO<sub>2</sub> in*  
744 *air, O<sub>2</sub> and N<sub>2</sub> near stp*, Atmospheric Environment, 32 (1998), pp. 1111–1127.
- 745 [26] M. K. NÆSS, *Mechanisms and Kinetics of Liquid Silicon Oxidation*, PhD thesis, Norwegian University of Science and  
746 Technology, 2013.
- 747 [27] M. K. NÆSS, G. TRANELL, J. E. OLSEN, N. E. KAMFJORD, AND K. TANG, *Mechanisms and kinetics of liquid silicon*  
748 *oxidation during industrial refining*, Oxidation of Metals, 78 (2012), pp. 239–251.
- 749 [28] K. OKUYAMA, Y. KOUSAKA, D. R. WARREN, R. C. FLAGAN, AND J. H. SEINFELD, *Homogeneous nucleation by continuous*  
750 *mixing of high temperature vapor with room temperature gas*, Aerosol Science and Technology, 6 (1987), pp. 15–27.
- 751 [29] S. E. PRATSINIS, *Simultaneous nucleation, condensation, and coagulation in aerosol reactors*, Journal of Colloid and  
752 Interface Science, 124 (1988), pp. 416–427.
- 753 [30] V. RAMAN AND R. O. FOX, *Modeling of fine-particle formation in turbulent flames*, Annual Review of Fluid Mechanics,  
754 48 (2016), pp. 159–190.
- 755 [31] D. RAMKRISHNA, *Population balances: Theory and applications to particulate systems in engineering*, Elsevier, 2000.
- 756 [32] A. SCHEI, J. K. TUSET, H. TVEIT, ET AL., *Production of high silicon alloys*, Tapir Trondheim, Norway, 1998.
- 757 [33] T. SETO, A. HIROTA, T. FUJIMOTO, M. SHIMADA, AND K. OKUYAMA, *Sintering of polydisperse nanometer-sized agglom-*  
758 *erates*, Aerosol Science and Technology, 27 (1997), pp. 422–438.
- 759 [34] S. SHEKAR, A. J. SMITH, W. J. MENZ, M. SANDER, AND M. KRAFT, *A multidimensional population balance model to*  
760 *describe the aerosol synthesis of silica nanoparticles*, Journal of Aerosol Science, 44 (2012), pp. 83–98.
- 761 [35] B. M. SLOMAN, C. P. PLEASE, AND R. A. VAN GORDER, *Asymptotic analysis of a silicon furnace model*, SIAM Journal  
762 on Applied Mathematics, 78 (2018), pp. 1174–1205.
- 763 [36] B. M. SLOMAN, C. P. PLEASE, R. A. VAN GORDER, A. M. VALDERHAUG, R. G. BIRKELAND, AND H. WEGGE, *A heat and*  
764 *mass transfer model of a silicon pilot furnace*, Metallurgical and Materials Transactions B, 48 (2017), pp. 2664–2676.
- 765 [37] B. M. SMIRNOV, *Nanoclusters and microparticles in gases and vapors*, vol. 6, Walter de Gruyter, 2012.
- 766 [38] S. STANKIC, M. COTTURA, D. DEMAILE, C. NOGUERA, AND J. JUPILLE, *Nucleation and growth concepts applied to the*  
767 *formation of a stoichiometric compound in a gas phase: the case of mgo smoke*, Journal of Crystal Growth, 329  
768 (2011), pp. 52–56.
- 769 [39] W. TSANG AND R. HAMPSON, *Chemical kinetic data base for combustion chemistry. part i. methane and related compounds*,  
770 Journal of Physical and Chemical Reference Data, 15 (1986), pp. 1087–1279.
- 771 [40] S. R. TURNS, *An Introduction to Combustion: Concepts and Applications*, McGraw-Hill Science Engineering, 2nd ed.,  
772 2000.
- 773 [41] G. D. ULRICH, *Theory of particle formation and growth in oxide synthesis flames*, Combustion Science and Technology,  
774 4 (1971), pp. 47–57.
- 775 [42] P. K. WANG, *Physics and dynamics of clouds and precipitation*, Cambridge University Press, 2013.
- 776 [43] D. R. WARREN AND J. H. SEINFELD, *Prediction of aerosol concentrations resulting from a burst of nucleation*, Journal of  
777 Colloid and Interface Science, 105 (1985), pp. 136–142.
- 778 [44] F. A. WILLIAMS, *Combustion theory*, CRC Press, 2018.
- 779 [45] K. ZHOU, A. ATTILI, A. ALSHAARAWI, AND F. BISETTI, *Simulation of aerosol nucleation and growth in a turbulent mixing*  
780 *layer*, Physics of Fluids, 26 (2014), p. 065106.

781 [46] A. ZUCCA, D. L. MARCHISIO, A. A. BARRESI, AND R. O. FOX, *Implementation of the population balance equation in CFD*  
782 *codes for modelling soot formation in turbulent flames*, Chemical Engineering Science, 61 (2006), pp. 87–95.